NOVA SCHOOL OF SCIENCE & TECHNOLOGY

DEPARTMENT OF PHYSICS

GIL DUARTE CABRITA DIAS ALVES

BSc in Biomedical Engineering

EVALUATING THE POTENTIAL OF GOLD-COATED NANODIAMONDS AS RADIOSENSITIZERS TO ENHANCE THE EFFECTIVENESS OF RADIATION THERAPY

MASTER IN BIOMEDICAL ENGINEERING

NOVA University Lisbon
September, 2025

NOVA SCHOOL OF SCIENCE & TECHNOLOGY

DEPARTMENT OF PHYSICS

EVALUATING THE POTENTIAL OF GOLD-COATED NANODIAMONDS AS RADIOSENSITIZERS TO ENHANCE THE EFFECTIVENESS OF RADIATION THERAPY

GIL DUARTE CABRITA DIAS ALVES

BSc in Biomedical Engineering

Adviser: Ana Lúcia Vital Belchior
Assistant Researcher, Centro de Ciências e Tecnologias Nucleares

Co-adviser: João Duarte Neves Cruz
Associate Professor, NOVA School of Science and Technology

Examination Committee

Chair: Célia Maria Reis Henriques
Associate Professor, NOVA School of Science and Technology

Rapporteur: Sandra Correia Vieira
Medical Physics Expert, Champalimaud Foundation

Adviser: Ana Lúcia Vital Belchior
Assistant Researcher, Centro de Ciências e Tecnologias Nucleares

MASTER IN BIOMEDICAL ENGINEERING

NOVA University Lisbon
September, 2025

Evaluating the Potential of Gold-coated Nanodiamonds as Radiosensitizers to Enhance the Effectiveness of Radiation Therapy

This document was created with the (pdf/Xe/Lua)LaTeX processor and the NOVAthesis template (v7.2.5) [1].

Para a minha família,

Acknowledgements

As I reach the conclusion of this academic journey, I wish to express my deepest gratitude to all those who contributed to its completion, supported me along the way, and without whom this achievement would not have been possible.

First and foremost, I would like to extend my sincere appreciation to my supervisors, Dr. Ana Belchior and Dr. Teresa Pinheiro at Instituto Superior Técnico, for their constant presence throughout the development of this work. Their willingness to provide guidance, clarify doubts, and share their invaluable knowledge was fundamental. Their contagious positivity and encouragement made this process lighter and more enjoyable, while their advice and direction ensured that I remained on the right path. I am equally grateful to my co-supervisor, Professor João Cruz at NOVA School of Science and Technology, for always being available to clarify any matter and for his readiness to provide assistance whenever needed.

I would also like to thank my colleagues Duarte Oliveira and Maria Lopes, who developed their theses in the same laboratory as mine. Their insights, shared perspectives, and good spirits created a supportive and welcoming environment, which made these past months much more pleasant.

To NOVA School of Science and Technology, my academic home for the past five years, I am deeply thankful for the education, experiences, and lasting friendships it has given me. To my friends, I owe my genuine gratitude for making this journey truly enjoyable, with moments that I will cherish for the rest of my life. To my girlfriend, Beatriz, whom I was fortunate to meet in my first year of university, I am profoundly grateful for your constant presence, love, and unwavering support. You have helped me grow as a person, and even when distance kept us apart, your wise advice and encouragement made me feel as if you were always by my side. I truly love you, and I could not be more thankful.

Finally, and most importantly, I would like to express my heartfelt gratitude to my family. None of this would have been possible without your unceasing care, belief in me, and encouragement to pursue my goals. Thank you for always being there, for supporting me in every way imaginable, and for giving me the strength to achieve this landmark. This thesis is for you.

”

“The ability to look deeply is the root of creativity. To see past the ordinary and mundane and get to what might otherwise be invisible.”

— Rick Rubin, The Creative Act: A Way of Being

Abstract

Cancer remains one of the leading causes of death worldwide, demanding continuous advancements in therapeutic strategies. Radiotherapy is a widely used treatment modality, but its effectiveness is often limited by radioresistant cancer cells and collateral damage to healthy tissues. To address this issue, radiosensitizers have emerged as a promising solution to enhance the effectiveness of radiotherapy by locally increasing the radiation-induced damage to cancer cells, while minimizing harm to the surrounding healthy tissues. In this context, gold nanoparticles have demonstrated a considerable radiosensitizing potential, while nanodiamonds have been explored for their fluorescence properties. Accordingly, recent investigations suggest that by combining these materials into gold-coated nanodiamonds (NDAus), it may be possible to integrate radiosensitization with bioimaging, enabling theranostic applications.

In this study, the radiosensitizing potential of NDAus was assessed in lung cancer cells exposed to γ-rays, X-rays and protons, delivered by a cobalt-60 irradiator, a clinical photon beam and a Van de Graaff accelerator, respectively. The cell survival response was evaluated using clonogenic assays, while fluorescence microscopy was employed to investigate mechanisms of DNA damage and repair, reactive oxygen species production and lipid droplets formation. Results demonstrated a predominant radiosensitizing effect at an NDAus concentration of 10 μg/mL under X-ray irradiation, with significant cell effects observed in the DNA damage and repair dynamics, as well as in the reactive oxygen species levels.

This work was distinguished with the Young Investigator Award at the 49^{th} conference of the European Radiation Research Society and was presented orally at both this meeting and the 11^{th} Congress of *Proteção Contra Radiações dos Países de Língua Portuguesa*. Additionally, the work was further discussed in the PIANOFORTE intensive course "Particle Irradiation: Molecular, Cellular and Tissue Effects".

Keywords: Gold-coated nanodiamonds, Nanoparticles, Radiosensitizers, Radiotherapy

Resumo

Atualmente, o cancro permanece uma das principais causas de mortalidade mundial, exigindo avanços contínuos no desenvolvimento de tratamentos mais eficazes. A radioterapia é um tipo de tratamento amplamente utilizado, mas a sua eficácia é frequentemente limitada pela presença de células cancerígenas radioresistentes e pelos efeitos colaterais que causa em tecidos saudáveis. Para ultrapassar estas limitações têm sido desenvolvidos radiossensibilizadores, compostos capazes de amplificar localmente os efeitos biológicos da radiação, minimizando os efeitos nocivos nos tecidos saudáveis. Neste contexto, as nanopartículas de ouro demonstram um potencial radiossensibilizador considerável, enquanto os nanodiamantes têm sido explorados pelas suas propriedades óticas. Assim, a combinação destas características em nanodiamantes revestidos de ouro (NDAus) surge como uma estratégia promissora para aplicações teranósticas.

Este estudo teve como objetivo avaliar o potencial radiossensibilizador dos NDAus em células de cancro do pulmão quando expostas a raios γ, raios X e protões, produzidos por uma fonte de cobalto-60, um feixe clínico e um acelerador *Van de Graaff*, respetivamente. A sobrevivência celular foi analisada através de ensaios clonogénicos, enquanto os mecanismos de dano e reparação do ADN, produção de espécies reativas de oxigénio e formação de vesículas lipídicas foram analisados por microscopia de fluorescência. Os resultados demonstraram um efeito radiossensibilizador predominante para células incubadas com NDAus a uma concentração de 10 μg/mL e expostas a raios X, com efeitos celulares significativos ao nível do dano e capacidade de reparação do ADN, bem como na produção de espécies reativas de oxigénio.

Este trabalho foi distinguido com o prémio de jovem investigador na 49ª conferência da *European Radiation Research Society*, contando com uma apresentação oral na mesma e no 11º congresso de Proteção Contra Radiações dos Países de Língua Portuguesa. Para além disso, contou ainda com a participação no curso intensivo "*Particle Irradiation: Molecular, Cellular and Tissue Effects*" da associação *PIANOFORTE*.

Palavras-chave: Nanodiamantes revestidos de ouro, Nanopartículas, Radiossensibilizadores, Radioterapia

Contents

List of Figures

List of Tables

Abbreviations

53BP1 p53-binding protein 1 *(p. 7)*

AuNPs Gold Nanoparticles *(pp. 11, 12, 15, 27)*

BSA Bovine Serum Albumin *(p. 22)*

CTN/IST Campus Tecnológico e Nuclear/Instituto Superior Técnico *(pp. 19, 20, 26, 40)*

D Absorbed Dose *(p. 3)*
DDR DNA Damage Response *(p. 7)*
DR Dose Rate *(p. 3)*
DSB Double Strand Breaks *(pp. 7, 8, 13, 14, 16, 32)*

FBS Fetal Bovine Serum *(p. 18)*

H-NDs Hydrogenated-Nanodiamonds *(p. 14)*

LD Lipid Droplets *(pp. 8, 22, 23, 30, 36–38, 40)*
LINAC Linear Accelerator *(pp. 9, 20, 40)*
LQM Linear-Quadratic Model *(pp. 16, 17, 21, 25, 27, 29)*

MID Mean Inactivation Dose *(p. 17)*

NDAus Gold-coated Nanodiamonds *(pp. 2, 15, 18, 19, 24–26, 28–40)*
NDs Nanodiamonds *(pp. 13–15, 18, 26, 28, 39)*
NPs Nanoparticles *(pp. 11, 14)*
NV Nitrogen-Vacancy *(p. 13)*

OX-NDs Oxidized-Nanodiamonds *(pp. 14, 18, 28)*

PBS Phosphate-Buffered Saline *(pp. 19, 21–23)*
PE Plating Efficiency *(pp. 16, 26)*
PFA Paraformaldehyde *(pp. 22, 23)*
PIXE Particle-Induced X-ray Emission *(pp. 15, 19)*

RBE Relative Biological Effectiveness *(p. 17)*
ROS Reactive Oxygen Species *(pp. 7, 8, 14, 22, 23, 30, 33–38, 40)*

SEM Scanning Electron Microscopy *(p. 15)*
SER Sensitizer Enhancement Ratio *(p. 17)*
SF Survival Fraction *(p. 16)*
SOBP Spread-Out of Bragg Peak *(p. 11)*
SSB Single Strand Breaks *(pp. 7, 8, 16)*
STIM Scanning Transmission Ion Microscopy *(p. 15)*

1 Introduction

1.1 Context and Motivation

Cancer is a disease characterized by the uncontrolled growth and division of abnormal cells, which can then spread to other parts of the body, and is currently one of the leading causes of death globally. In 2022, there were an estimated 9.7 million cancer deaths, with lung cancer being the most common type registered, accounting for approximately 1.8 million deaths worldwide [2].

In its early stages, cancer develops from the transformation of normal cells into tumoral cells, often resulting from the interaction between an individual's genetic factors and different external agents. In fact, genetic content plays a major role in the development of this disease, since it is caused by changes to genes that regulate cellular processes, in particular cell growth and division [3]. Moreover, according to the World Health Organization, such changes may be influenced by tobacco use, alcohol consumption and unhealthy dietary habits, as they are among the primary risk factors for cancer [4]. These findings highlight the critical importance of adopting preventive behaviors to reduce the likelihood of developing the disease, which still lacks a definitive cure.

Current approaches to cancer treatment are broad and depend on the type, stage and characteristics of the cancer, as well as the patient's health condition. The most common treatments include surgery, chemotherapy and radiotherapy, which, in many cases, are used in combination to achieve more effective outcomes [5].

In this work, radiotherapy will be the main treatment under investigation, which uses high doses of radiation to precisely target and kill cancer cells. This is achieved through the interaction between radiation and matter, in particular cells and their constitutes, which may lead to the development of radiation-induced biological effects. These effects, in turn, are classified as direct and indirect, ultimately triggering a series of events that result in cellular changes, such as mutations or cell death. Thus, radiotherapy plays a significant role in tumor reduction, thereby enhancing survival rates and improving the quality of life for cancer patients.

However, in lung cancer treatment, radiotherapy faces considerable challenges due to the proximity of tumors to vital structures, such as the heart, esophagus and spinal cord, which restricts the amount of radiation that can be safely delivered to the patient. In addition, lung cancer cells may exhibit varying degrees of radioresistance, which compromise the treatment efficacy and contribute to disease recurrence [6, 7].

Therefore, there is a need to improve current therapies in order to minimize the radiation damage in healthy tissues, improve the treatment response in radioresistant cancer cells and decrease the prescribed dose to patients. This can be achieved through radiosensitization, a process that combines radiotherapy with radiosensitizers, which are compounds capable of locally amplifying radiation-induced indirect biological effects. By this means, cancer cells will become more sensitive to radiotherapy, leading to improved clinical outcomes in cancer treatment.

Among the various radiosensitizers currently under investigation, gold-coated nanodiamonds (NDAus) are emerging as promising multifunctional material due to their potential to combine radiosensitization with imaging properties, acting simultaneously as a therapeutic and diagnostic approach [8]. Accordingly, the central focus of this research concerns the evaluation of the potential of NDAus as radiosensitizers to enhance the effectiveness of radiotherapy, considering the limited understanding of the radiosensitizing effects of such particles.

1.2 Objectives

The aim of the work presented in this thesis was to conduct an in vitro study of the radiosensitizing mechanisms of NDAus on A549 lung cancer cells when exposed to different types of radiation, namely γ-rays, X-rays and protons.

To achieve this objective, a systematic approach was developed, beginning with the evaluation of the NDAus uptake by A549 cells. This represents an essential step to validate the attribution of subsequent experimental observations and interpretations to the presence of NDAus. Following the NDAus cellular uptake, the investigation focused on the assessment of cell survival in response to the combined treatment of NDAus and radiation, providing quantitative insights into radiosensitizing capability of these nanoparticles. In parallel, a comprehensive examination of the radiobiological endpoints associated to cellular damage was performed under the same experimental conditions, aiming to elucidate the underlying biological mechanisms triggered by the presence of NDAus and radiation.

Hence, this study is expected to provide important insights into the added value of NDAus as a radiosensitizing strategy to make radiotherapy more effective.

The research work described in this dissertation was carried out in accordance with the norms established in the ethics code of Universidade Nova de Lisboa. The work described and the material presented in this dissertation, with the exceptions clearly indicated, constitute original work carried out by the author.

2

Theoretical Background

2.1 Radiation Physics

The concept of radiation refers to energy emitted from a source that is transmitted through space or matter. This radiation can then deposit its energy by interacting with matter through which it passes [9]. For the purpose of therapy, it can be classified as electromagnetic radiation, based on photons, such as γ-rays and X-rays, and particulate radiation, which includes electrons, protons, neutrons and other heavier particles [10].

To quantify the energy deposited in matter it is relevant to introduce the physical quantity absorbed dose (D), defined by equation (2.1):

$$D = \frac{d\bar{\varepsilon}}{dm} \tag{2.1}$$

where $d\bar{\varepsilon}$ is the mean energy imparted by radiation to matter of mass dm. The SI unit is Gray (Gy) and has a meaning of 1 Joule of absorbed energy per kilogram of matter. Closely related to this definition is the dose rate (DR), which represents the dose delivered per unit of time. It is expressed in equation (2.2) as:

$$DR = \frac{dD}{dt} \tag{2.2}$$

where dD is the incremental dose delivered during the time interval dt, expressed in the SI unit Gray per second (Gy/s). In addition, it is often useful to introduce the quantity particle intensity ($\dot{N}$), defined in equation (2.3) as the number of radiation particles passing during a given time interval:

$$\dot{N} = \frac{dN}{dt} \tag{2.3}$$

where dN is the increment of the particle number in the time interval dt, expressed in the unit (s^{-1}).

Moreover, the processes through which the various types of radiation interact and deposit energy in matter are different and shall be explained in the following sections. For the purpose of this study, the main focus will be on photons and charged particles, in particular electrons and protons.

2.1.1 Photons Interactions with Matter

Photons interactions with matter can be divided into two steps. The first step regards the energy transfer between photons and electrons or nuclei, where the former can be absorbed or scattered. In the second step, the charged particles that received the photon energy may deposit it in the surrounding medium, through interactions with other electrons or nuclei [11].

This statement is critical to understand that photons are indirectly ionizing radiation, since they do not deposit energy directly in matter. Instead, they transfer it to secondary charged particles that will then deposit it in the medium.

Furthermore, depending on the atomic number (Z) of the absorber and the photon energy, the most probable interactions of photons with matter are the photoelectric effect, Compton effect and pair production [12]. The probability of these interactions is shown in figure 2.2.

2.1.1.1 Photoelectric Effect

The photoelectric effect is a process in which an incident photon transfers its entire energy to an atomic electron, typically from an inner shell, ionizing the atom. The ejected electron, called photoelectron, creates a vacancy in the inner shell, which is subsequently filled by an electron from an outer shell. This transition results in the emission of a characteristic X-ray photon or an Auger electron (see figure 2.1A–C) [12].

Consequently, this effect produces secondary electrons, including photoelectrons and Auger electrons, as well as characteristic X-rays photons. The latter may interact with matter again, generating additional secondary electrons in a cascading ionization process, which will contribute to the absorbed dose.

2.1.1.2 Compton Effect

The Compton effect involves a photon transferring part of its energy to an atomic electron, usually in an outer shell, which recoils and is ejected from the atom. This interaction produces a scattered photon with reduced energy and new direction, and a recoil electron with a fraction of the initial photon energy (see figure 2.1D) [12].

2.1.1.3 Pair Production

In the process of pair production, a high-energy photon interacts with the Coulomb nuclear field of an atom and is completely absorbed, generating an electron-positron pair. For this reaction to occur, the photon energy must exceed 1.022 MeV, which is equivalent to the rest energy of the electron-positron pair (see figure 2.1E) [12].

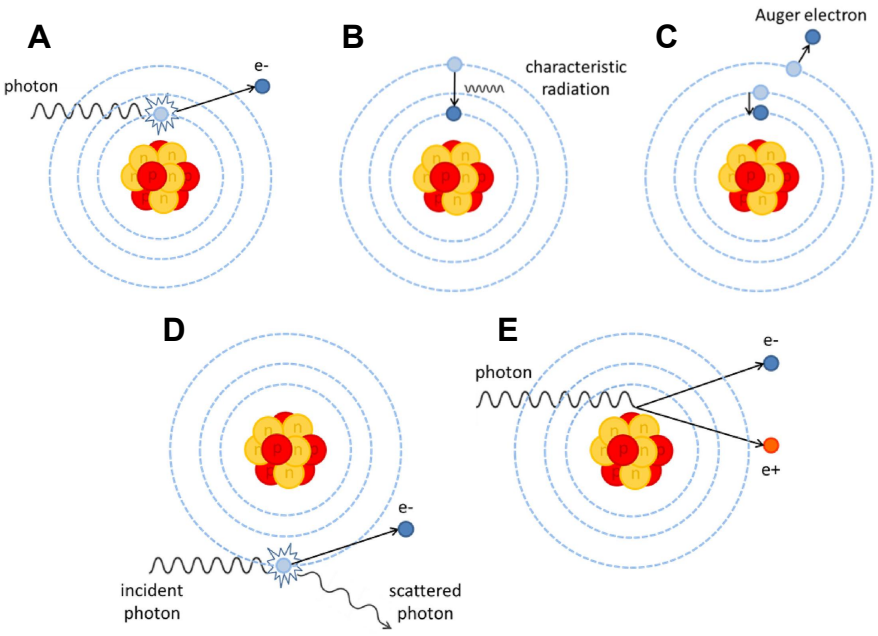

Figure 2.1: **Schematic representation of the interactions of photons with matter. (A)** Photoelectric effect with the emission of **(B)** a characteristic X-ray and **(C)** an Auger electron. **(D)** Compton effect and **(E)** the pair production process. Adapted from [12].

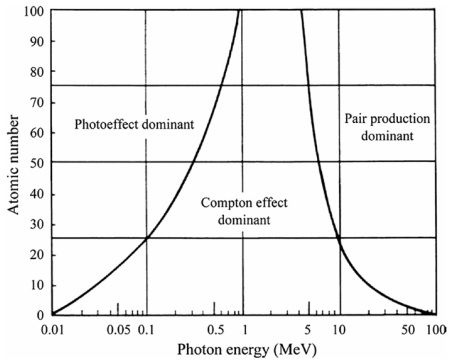

Figure 2.2: **The relative predominance of the three main photon interactions with matter according to the atomic number of the absorber and the photon energy.** Adapted from [13].

2.1.2 Charged Particles Interactions with Matter

As previously described, particulate radiation consists, in general, of energetic charged particles, such as electrons and protons. The electric field around such particles causes them to interact with other charges in the surrounding medium, making them more efficient at directly depositing energy in matter, since they will continuously lose energy while attracting or repelling other charged particles along their path [9].

In clinical applications, the most relevant processes through which charged particles interact with matter are excitation, ionization and the production of Bremsstrahlung radiation, with the latter being negligible for protons and heavier particles.

2.1.2.1 Excitation

In this process, an incident charged particle interacts with an atomic electron and transfers part of its energy, exciting the atomic electron to a higher energy state, which will later return to its ground state by emitting a photon (see figure 2.3A) [14].

2.1.2.2 Ionization

This process refers to a travelling charged particle that interacts with an atomic electron and transfers a fraction of its energy, ejecting it from its orbit and ionizing the atom. If the ejected secondary electron has enough energy to continue and cause further ionization, it is called delta ray (see figure 2.3B–C) [14].

2.1.2.3 Production of Bremsstrahlung Radiation

The Bremsstrahlung radiation may be produced when an electron passes close enough to an atom's nucleus, generating a deflection on the electron's path. This causes a rapid deceleration of the electron followed by a loss of energy, which is then emitted as a photon (see figure 2.3D) [14].

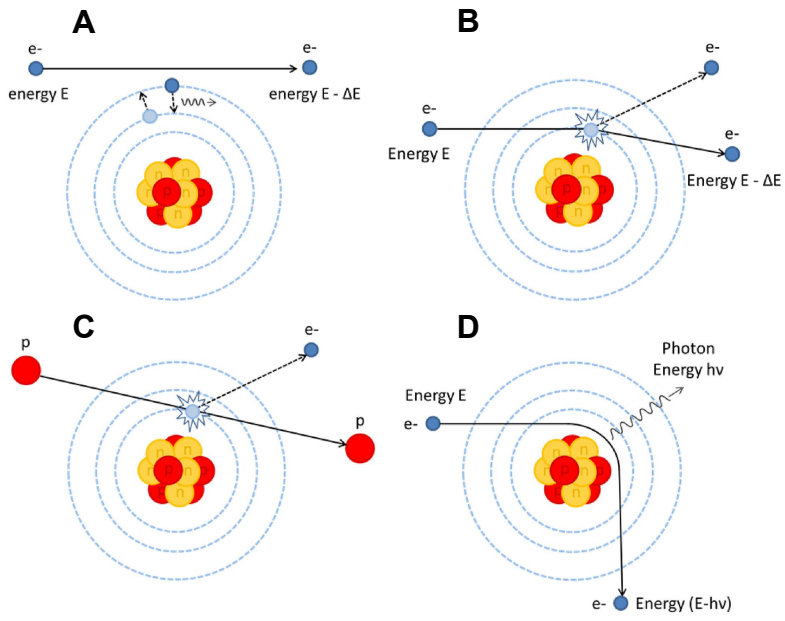

Figure 2.3: **Schematic representation of the interactions of charged particles with matter. (A)** Excitation and **(B)** ionization of an atomic electron by a travelling electron. **(C)** Ionization of an atomic electron by a travelling proton. **(D)** Production of Bremsstrahlung radiation by a travelling electron. Adapted from [14].

2.2 Radiobiology

In the context of radiotherapy, the physical processes described in section 2.1 will take place in biological systems, namely in cells and their constitutes, which may lead

to the development of radiation-induced biological effects. These can be classified as direct effects, when the interacting particle directly breaks a molecular bond of a cellular component, or indirect effects, when the interacting particles generate in the cellular medium chemically reactive species, which diffuse and may in turn interact with other cellular components (see figure 2.4). Consequently, both processes result in a series of events that lead to modifications in the cell, such as mutations or cellular death.

2.2.1 Direct Effects

2.2.1.1 DNA Damage

The part of the cell which is most sensitive to radiation damage is the DNA, a molecule that codifies the genetic information of the organism.

When radiation interacts directly with DNA it may ionize it, resulting in different types of DNA damage, such as single strand breaks (SSB) and double strand breaks (DSB), among others [15]. These lesions compromise the structure and function of the genetic material, with DSB being the most lethal.

Following a DSB, the histone variant H2AX is rapidly phosphorylated near the break site, resulting in γ-H2AX. This modification propagates along the surrounding DNA region and acts as a signal to recruit DNA damage response (DDR) proteins. Among these, the p53-binding protein 1 (53BP1) binds to γ-H2AX, acting as a platform for recruiting other DDR proteins and guiding the repair pathway selection. Accordingly, the accumulation of γ-H2AX and 53BP1 near the DSB leads to the formation of nuclear foci, which can be visualized through fluorescence microscopy [16, 17].

Furthermore, if the repair is successful, the γ-H2AX is dephosphorylated and the foci disappears. However, misrepaired lesions may lead to mutations, while unrepairable damage can ultimately result in cell death.

2.2.2 Indirect Effects

2.2.2.1 Production of Reactive Oxygen Species

To analyze the interactions between radiation and cells, it is pertinent to consider the radiochemical reactions occurring in water, given that it represents over 70% of the cellular content.

When a water molecule is ionized by radiation, it originates H_2O^+ and a free electron that, when trapped among water molecules, is designated as solvated electron (e_{aq}^-) (see equation (2.4)). The ionized water molecule can then divide and react with other water molecules to form reactive oxygen species (ROS) (see equation (2.5)), such as the hydroxyl radical ($OH^\bullet$), superoxide radical ($O_2^{\bullet-}$), hydrogen peroxide (H_2O_2), which are unstable molecules that contain oxygen.

$$H_2O \longrightarrow H_2O^+ + e^- \longrightarrow H_2O^+ + {e_{aq}}^- \tag{2.4}$$

$$H_2O^+ \longrightarrow OH^\bullet + H^+ \tag{2.5}$$

Additionally, when present in high concentrations, these species can induce significant cellular damage through oxidative stress. This is attributed to the ability of ROS to directly interact with DNA bases, causing structural changes, as well as SSB and DSB. Furthermore, ROS can attack mitochondrial membranes and proteins, disrupting the electron transport chain and consequently impairing ATP synthesis. Collectively, these effects compromise vital cellular processes, ultimately resulting in cell death [18, 19].

2.2.2.2 Lipid Damage

Along with the previously described interactions, ROS can also attack free fatty acids, which triggers a chain reaction of lipid peroxidation [18]. This process directly contributes to cellular damage by changing the structural integrity of polar lipid components, such as the cell membrane [20, 21].

To mitigate lipid toxicity, cells employ lipid droplets (LD), which are organelles with a neutral lipid core surrounded by a single phospholipid membrane, to sequester potentially toxic free fatty acids and convert them into less harmful neutral lipid forms. By storing fatty acids in inert forms, LD reduce the pool of lipids susceptible to peroxidation and act as a protective mechanism against oxidative stress [22–24].

Moreover, recent studies report that cancer cells present a higher number of LD compared to normal cells, and within tumors, cells with a higher number of LD exhibit greater survival after irradiation. This suggests that LD may contribute to radioresistance by creating a more tolerable oxidative microenvironment, thereby supporting tumor progression. Hence, LD represent a significant area of investigation for uncovering radioresistance mechanisms, which may, in turn, provide valuable insights into strategies for enhancing the sensitivity of cancer cells to radiotherapy [25, 26].

2.3 Radiotherapy

Radiotherapy takes into consideration the aforementioned physical and biological effects by using radiation beams to precisely target and kill cancer cells. To this end, it operates under the principle of maximizing the absorbed dose to the target volume while minimizing the damage to surrounding healthy tissues.

This type of treatment is critical given its ability to treat localized tumors, either by eliminating them or reducing symptoms in advanced cases. It can be used both to shrink tumors before surgery and to eliminate remaining cancer cells afterwards, improving the overall effectiveness of treatment [28]. Herein, some insights will be given on two distinct approaches to external beam radiation therapy: photon and proton beam therapy.

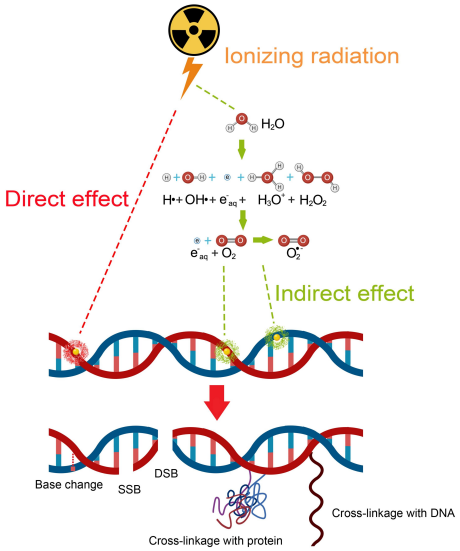

Figure 2.4: **Representation of the direct and indirect biological effects of radiation.** Direct effects occur when radiation directly damages DNA, resulting in cell death if the damage is unrepairable. Indirect effects occur when radiation ionizes water molecules to form ROS, which can then cause cellular damage. Both effects may lead to DNA damage such as SSB, DSB, DNA base damage and DNA-DNA or DNA-Protein crosslinks. Adapted from [27].

2.3.1 Photon Beam Therapy

Traditional radiotherapy employs photon beams for cancer treatment. One of the earliest and most used sources of photons is the cobalt-60 (^{60}Co), a radioactive isotope known as a reference radiation source. ^{60}Co decays by emitting an electron and two γ-rays with energies of 1.17 and 1.33 MeV, resulting in an average photon energy of 1.25 MeV. In this context, ^{60}Co irradiators are utilized as external beam radiotherapy units, using the emitted γ-rays as the photon beam [9, 29].

However, ^{60}Co units have been replaced with linear accelerators (LINAC), which make use of high energy electrons travelling in an oscillating field to produce X-rays. Unlike the γ-rays from ^{60}Co, X-rays produced by LINAC offer greater penetration since their energy can be adjusted depending on the depth of the tumor, ranging from 4 to 25 MV, to make sure the absorbed dose on the target volume is optimized [30]. To better understand the behavior of the dose distribution in depth, it is relevant to introduce the depth dose curves of the aforementioned radiation types, represented in figure 2.5.

In line with figure 2.5, X-ray beams above 6 MV are used for treating deep seated tumors, since the dose maximum is at a few centimeters in depth, and not at skin depth as it occurs for lower energy X-rays or ^{60}Co γ-rays. However, after the dose maximum, the curve shows an exponential decrease that may contribute to a non-negligible dose to healthy tissues [32].

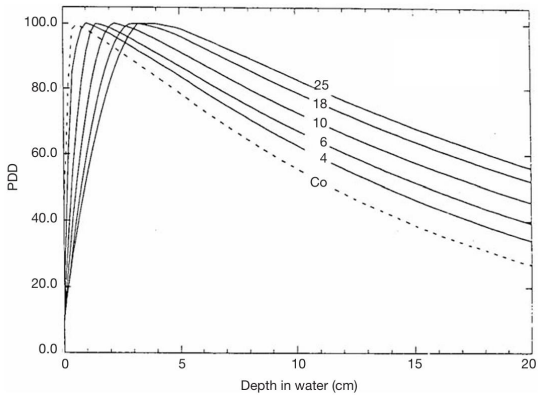

Figure 2.5: **Percentage Depth Dose (PDD) curves for ^{60}Co γ-rays and X-ray beams ranging from 4 to 25 MV**. Adapted from [31].

2.3.2 Proton Beam Therapy

Proton therapy is an emerging technique that uses cyclotrons to accelerate protons up to 250 MeV for cancer treatment. The advantage of the irradiation with protons compared to traditional radiotherapy is based on the different dose deposition in tissues, presented in figure 2.6A [33].

While photons demonstrate an exponential decrease of absorbed dose in depth, a monoenergetic proton beam exhibits a depth dose curve characterized by an initial plateau, a sharp increase up to a maximum at the end of the proton's range, followed by a steep fall-off. In this context, the depth of the maximum dose deposition depends on the initial energy of the proton beam [10].

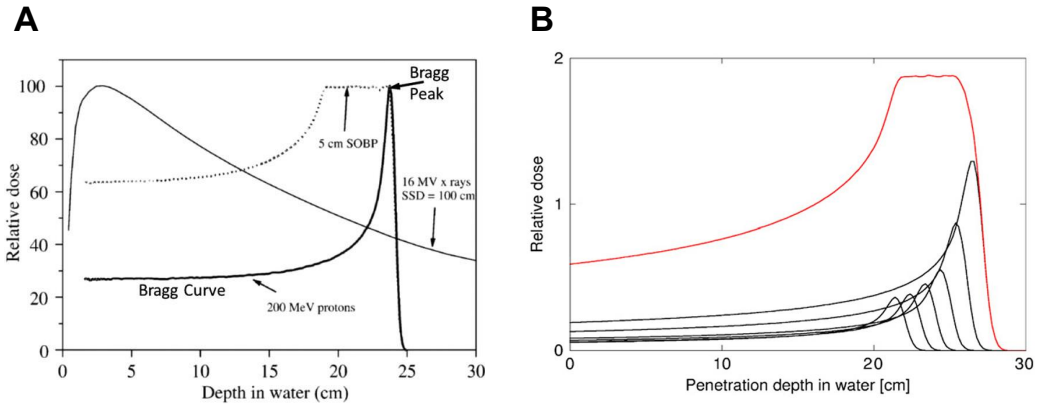

Figure 2.6: **Depth dose curves of proton beams. (A)** Depth dose curves of 200 MeV protons compared to 16 MV photons. **(B)** Representation of the SOBP with decreasing proton beam energies. Adapted from [34, 35].

The maximum of this curve is known as Bragg peak, but since its width, for a monoenergetic proton beam, is too narrow to cover most clinical targets, multiple beams of decreasing energy are used to create a wider area of high dose. The sum of these beams

is known as the spread-out of Bragg peak (SOBP), visible in figure 2.6B. Thus, the width of the SOBP is designed to cover the target volume, allowing deposition of maximum energy at the tumor site while minimizing the damage to healthy tissues along their path [10, 28].

2.4 Radiosensitizers

Although radiotherapy is a highly localized treatment, ionizing radiation must traverse the patient to reach the target, inevitably depositing dose in healthy tissues. Furthermore, if the treatment fails to eliminate all cancer cells, those that receive a lower dose may develop resistance to radiation. Consequently, higher doses may become necessary for treatment, leading to increased damage to the surrounding healthy tissue [36]. To address these challenges, various approaches to enhance the efficacy of radiotherapy have been recently explored, with particular emphasis on the integration of radiosensitizers in radiotherapy, as illustrated in figure 2.7.

Radiosensitizers are agents that locally increase the susceptibility of tumor cells to radiation-induced damage, improving their response to radiotherapy [37]. In general, nanoparticles (NPs) have acquired significant interest due to their physicochemical properties, which can be tailored to meet the requirements of radiosensitizers. Among different NPs classes, high-Z NPs, such as gold nanoparticles (AuNPs), have been explored as a way to enhance local radiation doses by taking advantage of their capability to attenuate radiation [38].

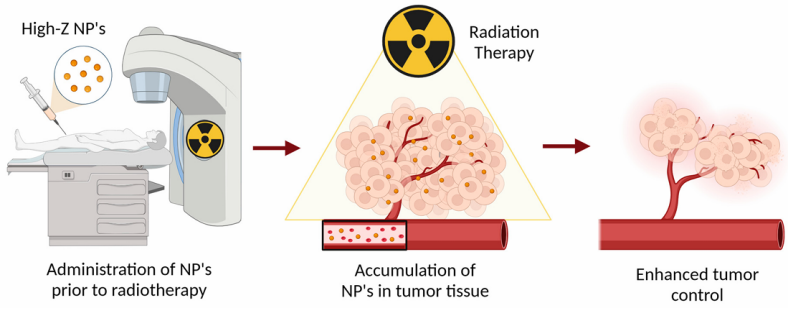

Figure 2.7: **Combination of high-Z radiosensitizers with radiotherapy to enhance local radiation doses and tumor control**. Adapted from [37].

Accordingly, within the scope of high-Z elements being investigated, such as silver, gadolinium and bismuth, gold stands out due to its good chemical stability, controllable size and shape, ease of surface functionalization and high biocompatibility [27, 39].

Studies have demonstrated a correlation between the size of AuNPs and their cellular uptake, with AuNPs in the mid-size range (near 50 nm) exhibiting the highest uptake when compared to smaller or larger sizes [40, 41]. Additionally, the concentration of AuNPs plays a crucial role in enhancing the locally absorbed dose, but it's also associated with cytotoxicity, as higher concentrations may increase the risk of cytotoxic effects. Hence,

it is paramount to find the balance between the dose enhancement effect and the risk of cytotoxicity [37, 42].

However, when taking all of these parameters into account, some results still lack consistency, as it is not clear which combination of parameters will provide the best radiosensitizing effects.

Another point to consider is the interaction between AuNPs and radiation, which is fundamental for better understanding the local dose enhancement effect. As aforementioned (see figure 2.2) the probability of the photoelectric effect increases with Z and decreases with the photon energy. Thus, when photons travel through tissue, which has a low Z, the photoelectric effect has a low occurrence probability. However, if the photon interacts with AuNPs present in the tissue, the photoelectric effect will be predominant, resulting in the emission of photoelectrons, X-rays and Auger electrons, which will contribute to the enhancement of local dose deposition and consequently to cellular damage, as presented in figure 2.8 [13]. Similarly, protons, by colliding with AuNPs, induce the generation of secondary electrons, photons and positrons, which will also contribute to cellular damage [43].

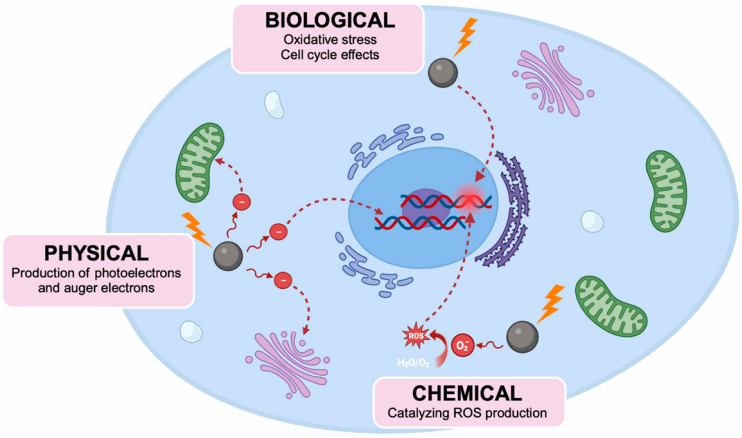

Figure 2.8: **Physical, chemical and biological mechanisms of high-Z NPs radiosensitization**. Adapted from [37].

Finally, the size and surface characteristics of the AuNPs can be adjusted to ensure that the dose is deposited mainly in tumor cells. Owing to the poor structural integrity of the tumor microenvironment, the reduced size of these particles enables their preferential accumulation in tumors compared to normal tissue, a phenomenon referred to as passive targeting. In contrast, active targeting can be achieved by functionalizing the surface of AuNPs with specific ligands, allowing particles to selectively bind to cancer cells overexpressing a particular surface receptor, ultimately resulting in their internalization via endocytosis [37].

3

State of Art

Nanodiamonds (NDs) are emerging as a promising material applicable to various technologies, owing to their unique properties including fluorescence, chemical stability, ease of surface functionalization, intrinsic biocompatibility and low toxicity [44].

Bioimaging is one of the fields in which NDs have been recently studied, focusing on their fluorescence properties. These arise from the presence of optically active defects that act as color centers, such as Nitrogen-Vacancy (NV) centers, which consist of a substitute nitrogen atom near to a vacancy defect [45]. These show intense and stable fluorescence in red wavelength when excited with green light, which makes them excellent for long-term cellular imaging [46–48]. Sturari et al. [49] performed the functionalization of NDs with hyaluronic acid–phospholipid conjugates (HA) to enhance their selectivity for cancer cells overexpressing specific HA cluster receptors (CD44), while taking advantage of their fluorescent imaging capabilities. Through confocal microscopy it was assessed that the functionalized NDs demonstrated active targeting in the presence of cancer cells expressing CD44, and that the main intracellular localizations were the nuclear and perinuclear regions, highlighting their suitability for nuclear targeting.

Along with bioimaging, NDs exhibit significant properties that justify further investigation regarding radiosensitizing applications. On that context, Mi et al. [50] developed a correlative iono-nanoscopy technique to image, localize and quantify fluorescent NDs at high resolution throughout a whole cell, taking advantage of a highly focused α-beam (see figure 3.1). Initially, results showed strong ionoluminescence emission of fluorescent NDs when excited with α-particles. Afterwards, HeLa cells were incubated with NDs and imaged in ionoluminescence and transmission-ion mode, resulting in a luminescence map that showed the biodistribution of the NDs and a density map that illustrated cellular structures. When overlaid, these allowed the localization and quantification of intracellular NDs. The radiosensitizing mechanisms were investigated through simulation and experimental irradiation of HepG2 cells incubated with NDs, using a proton beam. The outcome showed no radio-enhancement of DSB by NDs under proton irradiation, which suggests that the NDs radiosensitizing mechanisms may operate through alternative pathways other than damaging nuclear DNA.

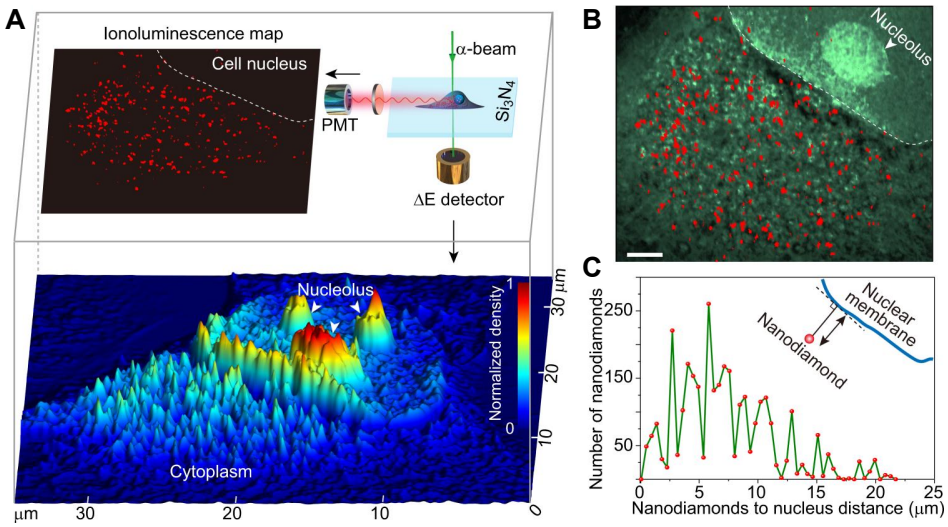

Figure 3.1: **Demonstration of the correlative ultrastructure and ionoluminescence imaging of HeLa cells with endocytosed NDs. (A)** Simultaneous acquisition of luminescence images of the nanodiamonds and 3D rendering of the cellular ultrastructure. **(B)** Overlay of the structural and luminescent images, showing the localization of NDs in the cell. **(C)** Measurement of the number of intracellular NDs in terms of their distance to the cell nuclear boundary. Adapted from [50].

On the other hand, Grall et al. [51] studied the effects of hydrogenated-NDs (H-NDs) on cancer cell radioresistance and reported that H-NDs exhibit a negative electron affinity, which confers high reactivity with oxygen species. Accordingly, their experiments established a higher generation of ROS when intracellular H-NDs were exposed to γ-rays as compared to radiation or H-NDs alone, resulting in a radiosensitizing effect with occurrence of DSB.

To further understand the controversies in NDs radiosensitizing mechanisms, a recent work published by Varzi et al. [52] investigated the NDs effects on cancer cell radiosensitivity with variations in size, surface modification and concentration of the NDs, as well as in the radiation energy. The surface modifications tested were with oxidized-NDs (OX-NDs) and H-NDs, which revealed opposite behaviors, with the latter enhancing radiosensitization due to its ability to transfer electrons to oxygen species in the cytoplasm, acting as a source of ROS. Focusing on H-NDs, differences in cell survival were observed with different energy beams. With X-rays at keV energies, which maximize radiosensitization for high-Z NPs based on the photoelectric effect, there weren't observed meaningful changes. However, with γ-rays at MeV energies, a significant decrease in cell survival was reported, improving radiosensitization with Compton effect as the predominant interaction. Additionally, the enhanced cell death was not associated with DNA damage, reinforcing the idea that alternative targets for nanoparticle-mediated radiosensitization should be explored in future studies.

Given the unique properties of both NDs and AuNPs previously described, some research groups are currently investigating the potential of the gold-coated nanodiamonds (NDAus) hybrid system [53]. In this regard, Mendes et al. [54] evaluated the stability of NDAus in cell culture medium, showing that these particles remain stable for a period of 24 hours. In addition, the cytotoxicity of NDAus in concentrations ranging from 10 to 100 μg/mL was assessed after 24 hours incubation in A549 cells, identifying concentrations of 10 and 20 μg/mL as optimal under these conditions. Furthermore, the cellular uptake of such nanoparticles was confirmed by scanning electron microscopy (SEM) images, as A549 cells incubated with NDAus displayed typical morphology without signs of damage, alongside with visible NDAus aggregates both inside and outside the cells (see figure 3.2A). As well, nuclear microscopy techniques such as scanning transmission ion microscopy (STIM) and particle-induced X-ray emission (PIXE) were used to measure the distribution of gold in the cells, as a signature of the NDAus (see figure 3.2B).

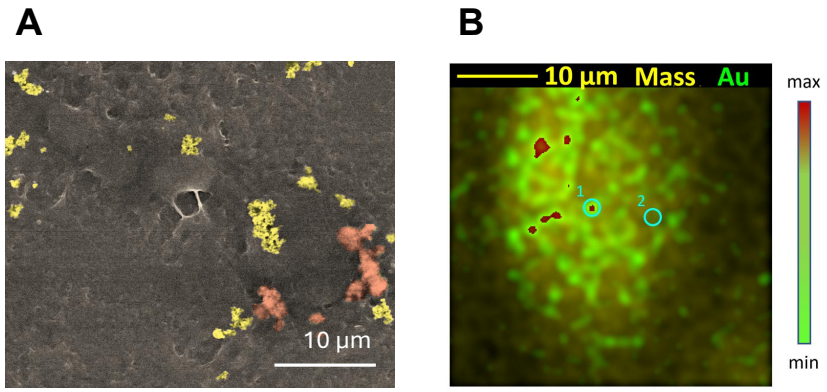

Figure 3.2: **Internalization of NDAus at a concentration of 20 μg/mL in A549 cells. (A)** SEM imaging of the NDAus distribution, with yellow indicating NDAus outside cells and orange representing NDAus inside cells. **(B)** Superimposed nuclear microscopy images of mass density by STIM and gold distribution by PIXE, where the mass density is represented by a yellow gradient, and the gold distribution by a color scale ranging from green-low to red-high. Adapted from [54].

Similarly, Liu et al. [55] developed fluorescent nanodiamond-gold nanoparticles (FND-Au) for multimodal optical and electron microscopy cellular imaging. The research reported that FND-Au greatly enhanced image contrast and that the FND emission wasn't quenched by the AuNPs, enabling detailed studies inside cells ranging from whole-cell images, down to the tracking of individual particles in subcellular organelles, with single-particle resolution.

Although NDAus are highly promising in bioimaging, there are very few studies investigating their potential as radiosensitizers. Indeed, if NDAus successfully integrate these capabilities, they could act simultaneously as a therapeutic and diagnostic approach. Therefore, this study explores the NDAus radiosensitizing mechanisms in order to assess their potential for cancer treatment.

4

Models and Quantities

To evaluate cancer cell radiosensitivity, the clonogenic assay is considered a gold standard, as it measures the ability of a single cell to grow into a colony after irradiation, thereby quantifying cell survival [56]. In this context, the assay results are derived from two key parameters: the plating efficiency (PE) and the survival fraction (SF) [57]. The PE, as defined in equation (4.1), corresponds to the ratio between the number of colonies formed and the number of cells seeded.

$$PE = \frac{number\ of\ colonies\ formed\ (average)}{number\ of\ cells\ seeded} \tag{4.1}$$

Similarly, the SF expressed in terms of PE, for each condition (i.e., dose), is described in equation (4.2).

$$SF = \frac{number\ of\ colonies\ formed\ after\ irradiation\ (average)}{number\ of\ cells\ seeded \times PE} \tag{4.2}$$

The experimental data are then plotted as survival curves, with the survival fraction as a function of the absorbed dose. To mathematically describe this relation, the linear-quadratic model (LQM) is frequently employed, as defined by equation (4.3):

$$SF(D) = e^{-\alpha D - \beta D^2} \tag{4.3}$$

where α and β are parameters that describe cell radiosensitivity. Specifically, α (Gy^{-1}) is the linear coefficient associated with lethal damage, such as DSB, caused by a single incident particle. In contrast, β (Gy^{-2}) is the quadratic coefficient related to lethal damage arising from the combination of sublethal events, such as SSB, induced by multiple incident particles. Consequently, direct lethal events contribute to an initial linear component at low doses, while the accumulation of multiple sublethal events results in an increasing curvature. The survival curve can then be characterized by the α/β ratio (Gy), which corresponds to the dose at which the linear and quadratic components contribute equally to cell killing, and is commonly used to describe cellular radiosensitivity. Thus, cells with high α/β ratios exhibit a more constant rate of cell killing as the dose increases, while cells with low α/β ratios present a more pronounced curvature, with greater cell killing at higher doses (see figure I.1) [58].

Fitting the experimental data with the LQM allows the calculation of several quantities useful for comparing experimental conditions, such as radiosensitizer-treated versus control cells, or even treatments using different radiation modalities [59]. One such quantity is the mean inactivation dose (MID), defined as the average radiation dose required to inactive a cell. It can be mathematically described as the area under the survival curve, according to equation (4.4).

$$MID = \int_0^\infty SF(D)\, dD \tag{4.4}$$

The MID can be used to quantify the radiobiological impact of a given radiosensitizer by calculating the ratio between the MID of control cells (MID_{CTR}) and the MID of cells treated with radiosensitizers (MID_{RS}), which ultimately defines the sensitizer enhancement ratio (SER), in line with equation (4.5).

$$SER = \frac{MID_{CTR}}{MID_{RS}} \tag{4.5}$$

Alongside the SER, the dose modifying ratio ($DMR_{x\%}$) is another important quantity used to assess the extent to which a radiosensitizer modifies cellular radiosensitivity. It may be written as the ratio between the dose necessary to achieve a given survival fraction ($x\%$) in control cells (D_{CTR}) and the dose required to produce the same survival fraction in cells treated with radiosensitizers (D_{RS}), consistent with equation (4.6).

$$DMR_{x\%} = \frac{D_{CTR}}{D_{RS}} \tag{4.6}$$

Another key quantity for evaluating the variation in the radiobiological response of a radiosensitizer at a specific dose is the radiation enhancement ratio (RER_{xGy}). It can be formulated as the ratio between the survival fraction of control cells (SF_{CTR}) irradiated with a given dose (xGy) and the survival fraction of cells treated with radiosensitizers when irradiated with the same dose (SF_{RS}), represented in equation (4.7). In addition, this quantity is particularly relevant when considering a dose of 2 Gy, as it corresponds to the standard dose delivered in a single fraction of traditional radiotherapy, giving valuable insights for clinical studies.

$$RER_{x\text{Gy}} = \frac{SF_{CTR}}{SF_{RS}} \tag{4.7}$$

Extending this analysis, one can introduce the relative biological effectiveness (RBE), a significant quantity for expressing the cellular response to different radiation fields. Accordingly, it is defined in equation (4.8) as the ratio between the dose of a reference radiation (D_{REF}) required to produce a given biological effect and the dose of the test radiation (D_{TEST}) necessary to achieve the same effect, with ^{60}Co γ-rays designated as the reference radiation.

$$RBE = \frac{D_{REF}}{D_{TEST}} \tag{4.8}$$

Taken together, the quantities and models discussed will be employed to analyse the effect of NDAus on cancer cell radiosensitivity, using data obtained through the methodologies outlined in the following section.

5

Materials and Methods

5.1 NDAus Characterization

The NDs used in this study were thermally treated and provided by Dr. Federico Picollo, from the University of Turin. According to the procedure detailed in [52], commercial NDs with an average particle size of 50 nm were annealed for 2 hours at 800 °C in a nitrogen (N_2) atmosphere. Subsequently, the annealed NDs were oxidized in an air atmosphere at 500 °C for 12 hours, resulting in OX-NDs. The OX-NDs were then coated with gold using a green chemistry method based on *Nymphaea alba* root extracts, as described in [60], yielding the NDAus used in this work.

5.2 Cell Culture Conditions

The A549 lung carcinoma epithelial cell line was purchased from American Type Culture Collection. The standard culture medium used was Dulbecco's modified Eagle's medium (DMEM) supplemented with GlutaMAX, 10% of fetal bovine serum (FBS) and 1% of antibiotic-antimitotic solution, which contains streptomycin, penicillin and 25 μg/mL of amphotericin B, to address the residual fungal spores from the plant root extracts. The cells were kept in an incubator at 37 °C and 5% CO_2 with a humidified atmosphere (Heraeus, Germany). All the products for cellular studies were acquired from Gibco (Thermo Fisher Scientific), unless stated otherwise.

5.3 Cell Incubation

A549 cells were seeded in 24-well plates following standard cell culture techniques and allowed to adhere overnight. The cells were then incubated for 24 hours in medium containing NDAus at a concentration of 10 and 20 μg/mL. After incubation, the medium was replaced with fresh one, without NDAus, and the cells were prepared for irradiation.

5.4 Cellular Uptake

To assess the NDAus cellular uptake, the concentration of gold was determined in A549 cells following incubation in medium containing NDAus at a concentration of 10 μg/mL for 24h. After this period, cell pellets were obtained by centrifugation, washed with phosphate-buffered saline (PBS) to remove the culture medium and subsequently freeze-dried. Afterwards, the pellets were subjected to microwave-assisted acid digestion using a 1:3 molar ratio of nitric and hydrochloric acids, with yttrium added at a concentration of 1000 mg/L as an internal reference. The gold content was then analyzed by PIXE using a 2.0 MeV proton beam generated by the Van de Graaff accelerator at Campus Tecnológico e Nuclear/Instituto Superior Técnico (CTN/IST). Spectra analysis was performed using the GUPIXE software with concentrations expressed as μg/g of dry material and then converted to μg per 10^6 cells.

5.5 Irradiation Procedures

5.5.1 γ-rays

Cell irradiation with γ-rays was performed using the Precisa-22 experimental ^{60}Co irradiator (Graviner Manufacturing Company Ltd.) at CTN/IST. The irradiator contains four ^{60}Co sources enclosed in stainless steel cylinders, arranged in pairs on both sides of the chamber and moved by a pneumatic system (see figure 5.1A–B) [61]. For irradiation, the 24-well plates were placed on a rotating support (see figure 5.1C) to ensure uniform dose distribution, with doses ranging from 0.5 to 10 Gy delivered at a dose rate of 1 Gy/min, which was determined by the position of the support inside the chamber.

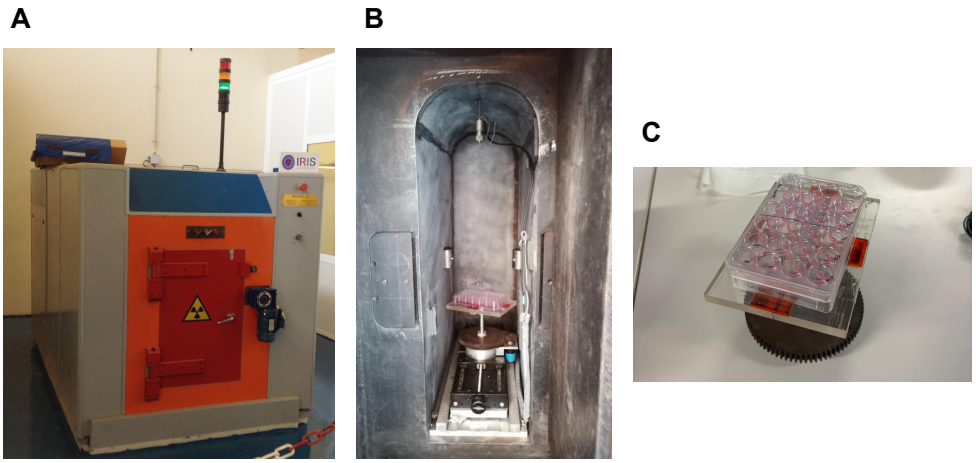

Figure 5.1: **γ-ray irradiation setup. (A)** External housing and **(B)** internal chamber of the Precisa-22 experimental ^{60}Co irradiator. **(C)** A 24-well plate placed on the rotating support.

5.5.2 X-rays

Cell irradiation with X-rays was conducted using a Varian Edge medical LINAC (Varian Medical Systems Inc.) at Champalimaud Foundation. A 6 MV uniform beam was employed in a posteroanterior direction (180º), specifically to prevent the beam from traversing air before reaching the cells (see figure 5.2A) [62]. To simulate the depth of the tumor within a patient, the 24-well plates were positioned inside a phantom at the LINAC isocenter, which was previously assembled using polystyrene slabs (see figure 5.2B) [63]. Most irradiations were performed using this setup and according to the dose distribution shown in figure 5.2C, with cells exposed to doses ranging from 0.5 to 8 Gy at a dose rate of 5.1 Gy/min.

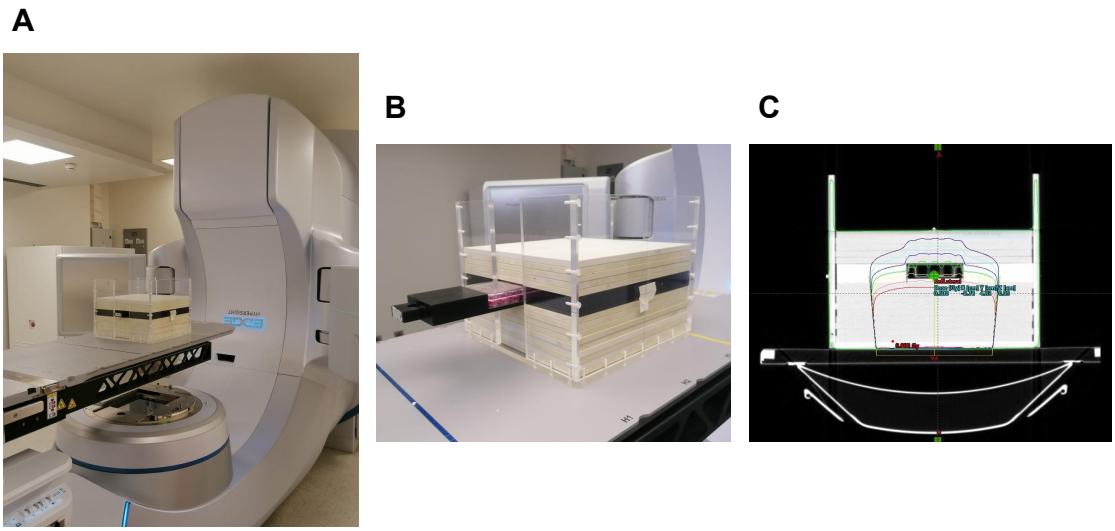

Figure 5.2: **X-ray irradiation setup. (A)** Varian Edge medical LINAC in the posteroanterior direction. **(B)** A 24-well plate placed on a polyoxymethylene drawer inside the phantom, between polystyrene slabs. **(C)** Dose distribution inside the phantom according to the treatment planning developed in the Eclipse software.

5.5.3 Protons

Cell irradiation with protons was conducted using the external microbeam facility of the Van de Graaff accelerator at CTN/IST (see figure 5.3A). Given the irradiation setup at the exit nozzle of the external microbeam, the 24-well plates used for cell seeding (described in section 5.3) were replaced by disks sealed with a mylar layer at the bottom and covered with a coverslip at the top (see figure 5.3B). Accordingly, a 2.0 MeV focused proton beam of 70 × 70 μm^2 was scanned across the cells, contained in 30 μL of culture medium within the disk. A proton intensity of 2–4 × 10^6 s^{-1} was used to achieve dose values comparable to the ones obtained in the aforementioned irradiation procedures, considering the air path and mylar length as attenuators. Cells were irradiated with three different dose values, corresponding to a beam exposure of 3, 6 and 10 seconds. To

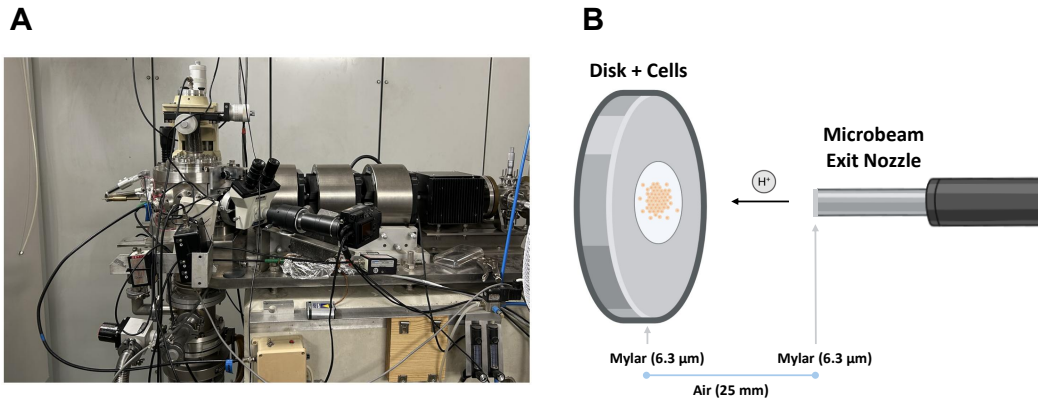

Figure 5.3: **Proton irradiation setup. (A)** External proton microbeam facility of the Van de Graaff accelerator. **(B)** Schematic representation of the cell irradiation (created with BioRender).

accurately obtain these values, Gafchromic XR-RV3 radiochromic films were irradiated under the same conditions and analysed using the Image J software to obtain the net optical density (netOD), a quantitative measure of how much radiation is absorbed [64]. The netOD was then correlated with the dose values using a previously established calibration curve (see annex I.2).

5.6 Clonogenic Assay

The clonogenic assay was used to evaluate the cell survival after irradiation. For γ-ray irradiation, cell incubation (see section 5.3) was previously performed by seeding approximately 100 cells per well in plates irradiated with doses between 0.5–2 Gy, and 200 cells per well in plates irradiated with doses between 4–10 Gy. However, for X-ray irradiation, approximately 100 cells were seeded per well in plates irradiated with doses between 0.5–1 Gy, 200 cells per well in plates irradiated with doses between 2–4 Gy and 400 cells per well in plates irradiated with doses between 6–8 Gy. Lastly, for the proton irradiation, each disk was seeded with approximately 2000 cells and, immediately after the irradiation, the cells were transferred to Petri dishes to continue the assay.

After irradiation, all cells were allowed to form colonies in the incubator for ten days, with the medium replaced with fresh one on the fifth day. The medium was then removed from all wells and Petri dishes, the colonies washed with PBS, fixed with an ice-cold solution of methanol and glacial acetic acid (3:1) and left to dry overnight. In the following step, the colonies were stained with 4% Giemsa solution, washed with tap water and left to dry. The detailed protocol for this assay is presented in section A.1.

Finally, the number of colonies was manually counted (see annex I.3), considering groups of more than 50 cells as colonies. Based on the results, the PE and SF were determined, and the data were fitted using the LQM.

5.7 Fluorescence Assays

Fluorescence assays were conducted right after γ-ray and X-ray irradiation to subsequently image the cells under the fluorescence microscope, focusing on the DNA damage and repair, ROS production and LD formation. For this purpose, cell incubation (see section 5.3) was previously carried out by seeding approximately 20000 cells onto round coverslips placed in each well.

5.7.1 DNA Damage and Repair Assays

DNA damage and repair sites were marked using a mouse anti-γ-H2AX (Ser139) primary antibody and a rabbit anti-53BP1 primary antibody, respectively. For fluorescence detection, an Alexa Fluor 488-conjugated anti-mouse secondary antibody was used to visualize γ-H2AX foci as green fluorescence upon excitation at a wavelength of 488 nm, while a Texas-Red-X-conjugated anti-rabbit secondary antibody was used to visualize 53BP1 foci as red fluorescence upon excitation at 595 nm. Additionally, 4,6-diamidino-2-phenylindole (DAPI) was used to stain the cell nuclei with blue fluorescence upon excitation at a wavelength of 405 nm.

After irradiation, cells were fixed with a 4% paraformaldehyde (PFA) solution and subsequently permeabilized with a 0.5% Triton X-100 solution. Afterwards, a solution of 2% bovine serum albumin (BSA) in PBS was added to each well, followed by the incubation with γ-H2AX and 53BP1 primary antibodies for 1h. Cells were then incubated with the fluorescent secondary antibodies for 1h and the nuclei were stained with DAPI. The coverslips containing cells were transferred onto clean slides, covered with mounting medium, sealed with coverslips and stored in the fridge until further microscopy analysis. All wells were washed with PBS after each solution was applied. The detailed protocol for this assay is presented in section A.2.

5.7.2 ROS Production Assay

ROS detection was performed using a 2',7'-dichlorodihydrofluorescein diacetate (DCFH-DA) probe, which is a non-fluorescent and cell-permeable compound. Once inside the cell, DCFH-DA is cleaved by esterases to form dichlorodihydrofluorescein (DCFH). Although still non-fluorescent, DCFH is highly sensitive to oxidation and can be converted by radiation-induced ROS into 2',7'-dichlorofluorescein (DCF), which emits an intense green fluorescence when excited at a wavelength of 485 nm. Thus, the intensity of the fluorescence signal correlates with the intracellular ROS levels [65].

After irradiation, a 4% PFA solution was added to each well. Then, cells were incubated with a DCFH-DA solution in the dark for 30 minutes and the nuclei were stained with DAPI. The coverslips containing cells were transferred onto clean slides, covered with mounting medium, sealed with coverslips and stored in the fridge until further microscopy

analysis. All wells were washed with PBS after each solution was applied. The detailed protocol for this assay can be found in section A.3.

5.7.3 LD Formation Assay

LD were marked using Nile Red (9-diethylamino-5H-benzo[a]phenoxazine-5-1), which is a lipophilic fluorescent dye that stains lipid-rich structures in cells. Upon entering the cell, it targets LD and accumulates in their neutral lipid cores, emitting a bright yellow-green fluorescence when excited at a wavelength of 450–500 nm. However, in more polar lipid environments, such as phospholipids, Nile Red emits a red fluorescence when excited at a wavelength of 515–560 nm. Hence, the yellow-green fluorescence provides a better selectivity for LD, while the red fluorescence detects polar lipids more effectively [66].

After irradiation, a 4% PFA solution was added to each well. Then, cells were incubated with a Nile Red solution in the dark for 30 minutes and the nuclei were stained with DAPI. The coverslips containing cells were transferred onto clean slides, covered with mounting medium, sealed with coverslips and stored in the fridge until further microscopy analysis. All wells were washed with PBS after each solution was applied. The detailed protocol for this assay is presented in section A.4.

5.8 Fluorescence Microscopy Imaging

A MetaSystems Axioplan 2 fluorescence microscope was employed to image all the cells subjected to the assays outlined in section 5.7. For the DNA damage and repair assays, cells were imaged using a ×63 objective lens. The resulting images were analyzed with counting pipelines in the CellProfiler software to identify and quantify DNA damage and repair foci, as well as their colocalization. For the ROS production and LD formation assays, cells were imaged using a ×20 objective lens. Both image types were subsequently analyzed using LIDROSIS, a software designed for automated image processing, segmentation and fluorescence analysis.

5.9 Statistical Analysis

Data analysis and graphic development was primarily performed using GraphPad Prism version 8.0.1 (GraphPad Software Inc., USA) and a p-value < 0.05 was considered as statistically significant. The clonogenic assay experimental data was evaluated by one-way ANOVA followed by Tukey's multiple comparisons test, and then fitted using the Linear Quadratic Cell Death Model. The impact of the transport on cell survival was assessed by unpaired t-tests. Fluorescence images related to ROS production and LD formation were analyzed using LIDROSIS, which integrates built-in statistical analysis.

6

Results and Discussion

6.1 Cellular Uptake

To begin with, it is essential to investigate the cellular uptake of NDAus, since it represents a prerequisite for understanding their potential role as radiosensitizers. To this end, gold was used as a marker to quantify the presence of these nanoparticles within cells. As expected, gold was not detected in control cells. On the other hand, cells incubated with NDAus at a concentration of 10 μg/mL presented a gold uptake of 2.2 ± 0.2 μg per 10^6 cells, indicating that approximately 20% of the NDAus available in the culture medium were internalized, as illustrated in figure 6.1.

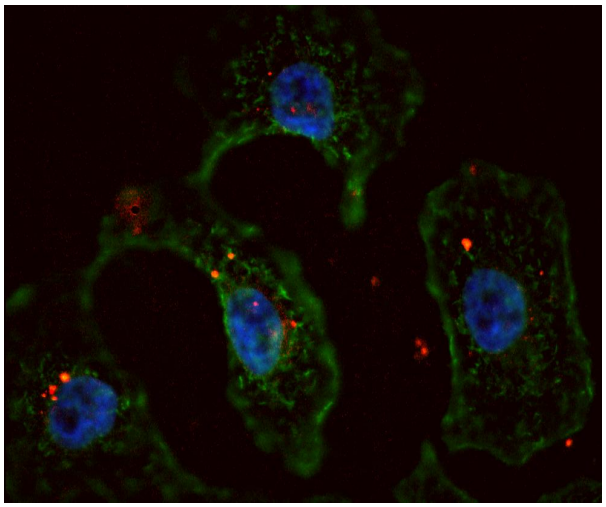

Figure 6.1: **Fluorescence microscopy image of NDAus at a concentration of 10 μg/mL internalized by A549 cells.** NDAus are shown in red, cell nuclei in blue and cell membrane in green.

Moreover, the cell matrix composition was analysed by quantifying the levels of each physiological element (see table I.1), and the results revealed no significant differences between cells incubated with NDAus and control cells.

6.2 Clonogenic Assay

6.2.1 γ-rays

Having established the NDAus internalization, control cells and those incubated with NDAus at concentrations of 10 and 20 μg/mL were irradiated with γ-rays at doses ranging from 0.5 to 10 Gy. Three independent assays were performed, and the corresponding survival fractions for each condition are presented in table I.2.

The survival fractions were then plotted as a function of the absorbed dose and subsequently fitted using the LQM, yielding the survival curves shown in figure 6.2. It is worth noting that, due to statistical differences observed in some values across the various assays, those data points were not considered for the LQM fitting.

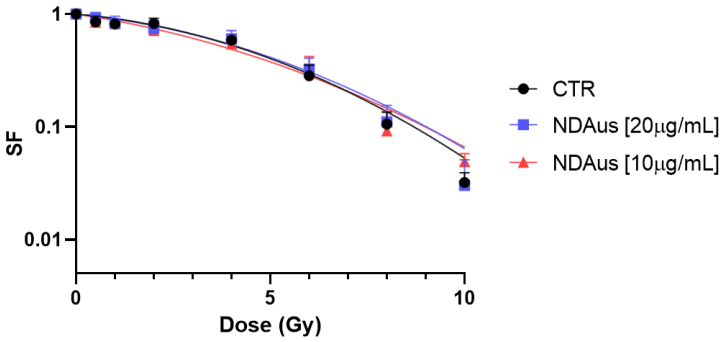

Figure 6.2: **Survival curves of A549 control cells and those incubated with NDAus at concentrations of 10 and 20 μg/mL after irradiation with γ-rays at doses ranging from 0.5 to 10 Gy.**

Afterwards, the LQM parameters described in chapter 4 were derived from the fit and are presented in table 6.1.

Table 6.1: **Values obtained with A549 control cells and those incubated with NDAus at concentrations of 10 and 20 μg/mL after γ-ray irradiation for the LQM parameters:** linear coefficient (α), quadratic coefficient (β), their respective 95% confidence intervals (95% CI), α/β ratio and R-squared (R^2).

LQM Parameters	CTR	NDAus [20 μg/mL]	NDAus [10 μg/mL]
α	0.069	0.078	0.119
95% CI (α)	0.011 to 0.127	0.013 to 0.144	0.042 to 0.197
β	0.023	0.020	0.015
95% CI (β)	0.012 to 0.034	0.009 to 0.033	0.003 to 0.031
α/β	3.06	3.99	7.76
R^2	0.967	0.955	0.942

Although there is limited literature specifically addressing the irradiation of A549 cells with ^{60}Co γ-rays, the results obtained allow for the identification of relevant internal trends in the context of radiosensitization using a reference radiation source.

In this regard, the parameter α showed an increase in cells incubated with NDAus compared to the control, where control cells and those incubated with NDAus at concentrations of 10 and 20 μg/mL presented α values of 0.069, 0.119 and 0.078 Gy^{-1}, respectively. The increase was most pronounced at 10 μg/mL, suggesting that NDAus at this concentration enhance the contribution of direct lethal lesions. However, at 20 μg/mL, α also increased relative to the control but to a lesser extent than at 10 μg/mL, indicating that while radiosensitization is still present, the effect does not scale proportionally with concentration.

In contrast, the parameter β decreased in cells incubated with NDAus relative to the control, where control cells and those incubated with NDAus at concentrations of 10 and 20 μg/mL showed β values of 0.023, 0.015 and 0.020 Gy^{-2}, respectively. Although the reduction is moderate, this trend suggests a diminished contribution of multiple sublethal events to cell killing, which may reflect a shift toward the direct lethal damage in the presence of NDAus.

Consequently, the α/β ratio increased in cells incubated with NDAus, where control cells and those incubated with NDAus at concentrations of 10 and 20 μg/mL exhibited α/β values of 3.06, 7.76 and 3.99 Gy, respectively. Accordingly, the predominant radiosensitizing effect was observed at 10 μg/mL, where the survival response was dominated by the linear component, consistent with the expected behavior of high-Z nanoparticle radiosensitizers. However, at 20 μg/mL, the α/β ratio remained higher than control but was reduced compared to the 10 μg/mL condition, implying that higher concentrations of NDAus may not linearly translate into greater radiosensitization. Similar trends have been described in the nanoparticle literature [67, 68], where optimal radiosensitizing concentrations are often observed. Beyond this optimal range, a higher amount of NDAus, and particularly the NDs component, may favor radiation absorption over the amplification of the radiation-induced biological effects, thereby reducing the overall radiosensitization.

6.2.2 X-rays

Following the same rationale as described for γ-rays, control cells and those incubated with NDAus at concentrations of 10 and 20 μg/mL were irradiated with X-rays at doses ranging from 0.5 to 8 Gy.

Since the X-ray irradiation was performed at Champalimaud Foundation, cells had to be transported from CTN/IST. To evaluate the impact of the transport on cell survival, the PE of two non-irradiated 24-well plates was assessed: one plate was transported from CTN to Champalimaud Foundation and back (CTR-TR), while the other remained in the incubator at CTN/IST (CTR-INC) (see figure I.4). The results showed no statistically significant differences between the CTR-TR and CTR-INC plates, so the average of the two was used as the non-irradiated condition in the survival fraction calculations. Again, three independent assays were conducted, and the respective survival fractions for each condition are presented in table I.3.

The survival fractions were then plotted as a function of the absorbed dose and subsequently fitted using the LQM, yielding the survival curves shown in figure 6.3, with statistically inconsistent outliers excluded from the fit.

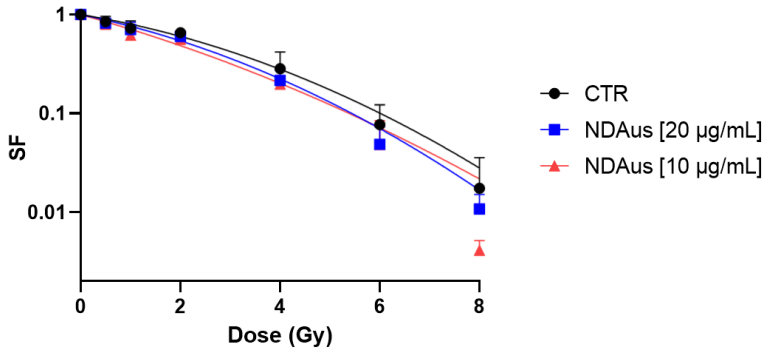

Figure 6.3: **Survival curves of A549 control cells and those incubated with NDAus at concentrations of 10 and 20 μg/mL after irradiation with X-rays at doses ranging from 0.5 to 8 Gy.**

After that, the LQM parameters were obtained from the fit and are presented in table 6.2.

Table 6.2: **Values obtained with A549 control cells and those incubated with NDAus at concentrations of 10 and 20 μg/mL after X-ray irradiation for the LQM parameters**: linear coefficient (α), quadratic coefficient (β), their respective 95% confidence intervals (95% CI), α/β ratio and R-squared (R^2).

LQM Parameters	CTR	NDAus [20 μg/mL]	NDAus [10 μg/mL]
α	0.190	0.238	0.323
95% CI (α)	0.089 to 0.291	0.141 to 0.333	0.224 to 0.420
β	0.032	0.034	0.020
95% CI (β)	0.007 to 0.065	0.008 to 0.069	-0.005 to 0.053
α/β	5.92	6.96	16.5
R^2	0.961	0.973	0.973

Early investigations suggested that tissues containing rapidly proliferating cells typically exhibit high α/β ratios, in the range of 7–10 Gy. Since cancer is characterized by uncontrolled growth and division of cells, it was initially assumed that cancer cells would present α/β ratios close to 10 Gy. However, recent studies have demonstrated that this is not always the case. In fact, considerable heterogeneity has been reported across different cancer cell lines irradiated with X-rays, with α, β and α/β values ranging from 0.05 to 0.5 Gy^{-1}, 0.01 to 0.07 Gy^{-2} and 0 to 10 Gy, respectively. Lung cancer cells, in particular, have yielded mixed results, with reported α/β ratios ranging from 2.2 to 9.4 Gy [58, 69, 70].

Furthermore, in the presence of radiosensitizers such as AuNPs, the radiosensitivity of A549 cells is strongly affected. This is typically reflected in alterations of the α and β parameters, with a clear increase in α relative to controls, while β remains less affected. As a result, the α/β ratio tends to increase under these conditions [71–74].

Consistent with the literature, the present work also demonstrated an overall increase in the parameter α in cells incubated with NDAus compared to controls, where control cells and those incubated with NDAus at concentrations of 10 and 20 μg/mL presented α values of 0.190, 0.323 and 0.238 Gy^{-1}, respectively. The higher α value was again observed at 10 μg/mL, suggesting that this concentration is particularly effective in amplifying lethal events. However, while α remained higher than control at 20 μg/mL, the effect was still reduced when compared to 10 μg/mL.

On the other hand, the parameter β did not follow the same trend, since control cells and those incubated with NDAus at concentrations of 10 and 20 μg/mL presented β values of 0.032, 0.020 and 0.034 Gy^{-2}, respectively. The reduction observed at 10 μg/mL suggests a diminished contribution of multiple sublethal lesions to cell killing, consistent with the radiosensitizing mechanism dominated by direct lethal damage. Conversely, a slight increase was observed at 20 μg/mL, which implies a greater role of multiple sublethal events in the survival response.

Consequently, the α/β ratio increased in the presence of NDAus, where control cells and those incubated with NDAus at concentrations of 10 and 20 μg/mL presented α/β values of 5.92, 16.5 and 6.96 Gy, respectively. The sharp increase at 10 μg/mL highlights the predominance of direct lethal damage over sublethal interactions, reinforcing the radiosensitizing effect also observed under γ-rays. At 20 μg/mL, although the α/β ratio remained higher than in control cells, the reduction compared to 10 μg/mL was much more significant, emphasizing the non-linear relationship between NDAus concentration and radiosensitization. In fact, an analogous behavior was reported by Varzi et al. [52], where DAOY cells incubated with OX-NDs at a concentration of 40 μg/mL and irradiated with X-rays exhibited a survival curve similar to the control cells. Together, these findings suggest that higher concentrations of NDs may translate into higher radiation absorption rather than amplifying the radiation-induced effects, through underlying mechanisms yet to be determined.

6.2.3 Protons

For proton irradiation, control cells and those incubated with NDAus at a concentration of 10 and 20 μg/mL were exposed to the proton beam for 3, 6 and 10 seconds. To determine the corresponding dose values, radiochromic films were irradiated under the same conditions (see figure I.5), yielding measured doses of 7.5 ± 0.8 Gy, 11 ± 2 Gy and 16 ± 2 Gy for irradiation times of 3, 6 and 10 seconds, respectively.

In the cell irradiation assays performed, the cells did not grow into colonies (see figure I.6), which may have been due to the use of a different reagent in the assembly of the disks employed in this the irradiation setup. Therefore, the survival fractions could not be calculated. Given the Van de Graaff accelerator's schedule and maintenance, this assay could not be repeated to date, so no results are available regarding the radiosensitizing potential of NDAus under proton irradiation.

6.2.4 Comparison of Different Radiation Type Effects

Having discussed the radiosensitizing effect of NDAus on cell survival under each radiation type individually, it is essential to compare the different modalities directly to assess whether the magnitude of the effect depends on the radiation field.

The analysis of the α/β ratios derived from the LQM provides an important first insight in terms of the NDAus concentration effects. For both γ-rays and X-rays, the presence of NDAus at 10 μg/mL produced a markedly higher α/β ratio compared to control cells and to the 20 μg/mL condition. Specifically, when irradiated with γ-rays, control cells exhibited an α/β ratio of 3.06 Gy, which increased to 7.76 Gy at 10 μg/mL, while the 20 μg/mL condition produced only a modest rise. Similarly, for X-ray irradiation, the control cells showed an α/β ratio of 5.92 Gy, which escalated to 16.5 Gy at 10 μg/mL, whereas the 20 μg/mL condition displayed again a reduced effect. Taken together, these results confirm that the concentration of 10 μg/mL is optimal for maximizing radiosensitization.

Building on this observation, further analyses were carried out to investigate the cellular response to both radiation types, for control conditions and in the presence of NDAus at 10 μg/mL, using the quantities defined in chapter 4 and summarized in table 6.3.

Table 6.3: **Values obtained with A549 control cells and those incubated with NDAus at 10 μg/mL after γ-ray and X-ray irradiation for the following quantities:** α/β ratio, survival fraction at a dose of 2 Gy (SF_{2Gy}), radiation enhancement ratio at a dose of 2 Gy (RER_{2Gy}), dose correspondent to a survival fraction of 50% ($D_{50\%}$), dose modifying ratio for a survival fraction of 50% ($DMR_{50\%}$), mean inactivation dose (MID), sensitizer enhancement ratio (SER) and the relative biological effectiveness for a survival fraction of 50% without ($RBE_{50\%\ CTR}$) and with NDAus ($RBE_{50\%\ NDAus}$).

Quantities	**Radiation Type**			
	γ-rays		**X-rays**	
	CTR	NDAus [10 μg/mL]	CTR	NDAus [10 μg/mL]
α/β	3.06	7.76	5.92	16.5
SF_{2Gy}	0.80	0.74	0.60	0.48
RER_{2Gy}	–	1.07	–	1.24
$D_{50\%}$	4.22	3.88	2.55	1.92
$DMR_{50\%}$	–	1.09	–	1.33
MID	4.55	4.35	2.93	2.43
SER	–	1.05	–	1.20
$RBE_{50\%\ CTR}$	1.66			
$RBE_{50\%\ NDAus}$	2.02			

Considering table 6.3, it is relevant to start by evaluating the intrinsic effectiveness of the two radiation modalities, taking into account their effect on control cells. In this context, the SF_{2Gy} was about 80% for γ-rays, while only 60% was observed for X-rays, implying that the latter produced a stronger effect in cell killing. This trend was consistent across other parameters, such as the $D_{50\%}$, with a value of 4.22 Gy for γ-rays compared to

2.55 Gy for X-rays, and the MID, with respective values of 4.55 Gy and 2.93 Gy. As well, the $RBE_{50\%\,CTR}$ reached approximately 1.66. Collectively, these findings confirm that X-rays are more effective in reducing cell survival than γ-rays, achieving the same biological endpoints at lower doses.

Moreover, upon addition of NDAus at 10 μg/mL, both radiation types demonstrated enhanced radiosensitization, but with different magnitudes. Accordingly, the RER_{2Gy} obtained for γ-rays was 1.07, but increased to 1.24 with X-rays, indicating that NDAus reduce the survival fraction at clinically relevant doses more effectively under X-ray exposure. Similarly, the $DMR_{50\%}$ was 1.09 for γ-rays compared to 1.33 for X-rays, and the SER was 1.05 for γ-rays against 1.20 for X-rays. Furthermore, the $RBE_{50\%\,NDAus}$ was approximately 2.02, emphasizing that the radiosensitizing effect of NDAus is markedly stronger under X-rays compared to γ-rays.

The differences observed between the two types of radiation can be attributed to their distinct photon energy spectra. While ^{60}Co γ-rays are emitted at two discrete energy values in the MeV range, the X-rays produced in the LINAC present a continuous energy spectrum extending up to 6 MeV. Hence, this broader distribution enables the interaction of photons with cell components and NDAus in a wider energy range, which may induce a higher secondary electron production, leading to greater cellular damage comparatively to γ-rays.

However, until this point, the processes through which NDAus at 10 μg/mL enhance cell killing under both γ-rays and X-rays remain to be characterized. In this regard, fluorescence microscopy assays were performed to investigate DNA damage and repair, ROS production, and LD formation, which together should provide a more comprehensive picture of the NDAus radiosensitizing mechanisms.

6.3 Fluorescence Microscopy Imaging

6.3.1 DNA Damage and Repair

6.3.1.1 γ-rays

As DNA is considered the most radiosensitive cellular target, the analysis of radiation-induced DNA damage and repair is fundamental in elucidating the mechanisms underlying the radiosensitizing effect of NDAus. To this end, A549 cells irradiated with 2 and 6 Gy of γ-rays were imaged (see figure 6.4A) and the γ-H2AX and 53BP1 foci were quantified, both in control conditions and in the presence of NDAus at 10 μg/mL (see figure 6.4B–D).

In a general trend, according to figure 6.4A, γ-H2AX and 53BP1 foci counts increased in a dose-dependent manner. This outcome was expected, as higher radiation doses deposit more energy within the cells, thereby increasing the probability of inducing DSB and consequently activating DNA repair mechanisms.

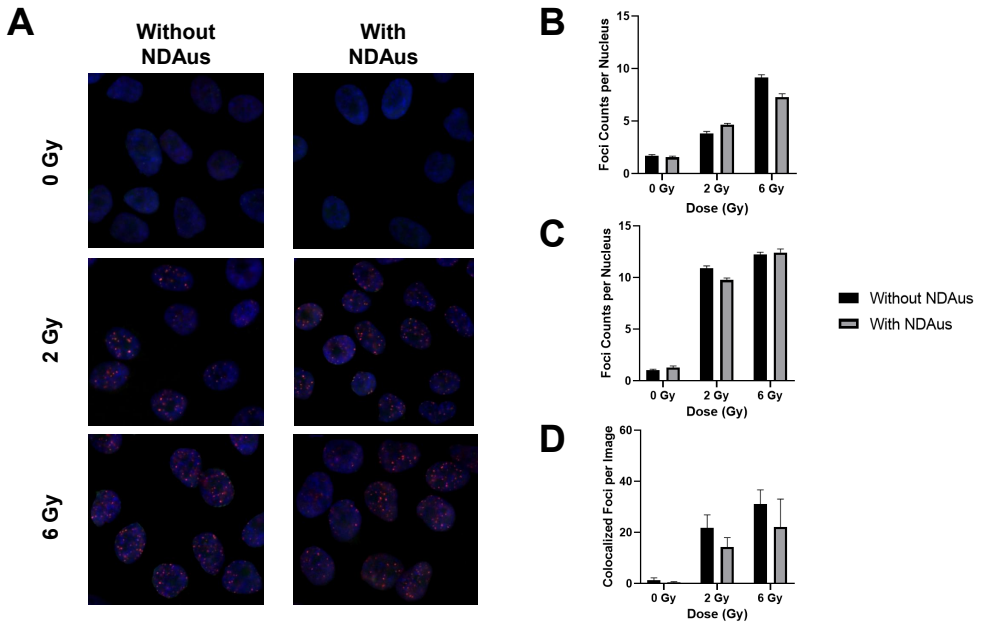

Figure 6.4: **DNA damage and repair foci following γ-ray irradiation. (A)** Fluorescence microscopy images of γ-H2AX and 53BP1 foci in control cells and those incubated with NDAus after irradiation with 2 and 6 Gy. **(B)** γ-H2AX foci counts per nucleus per dose. **(C)** 53BP1 foci counts per nucleus per dose. **(D)** Colocalized γ-H2AX and 53BP1 foci per image per dose.

Specifically, γ-H2AX foci counts (see figure 6.4B) showed a slight increase in the presence of NDAus at 2 Gy, suggesting that these particles may enhance DNA damage. In contrast, at 6 Gy, a reduction in the number of γ-H2AX foci was observed. This decrease may be attributed to the induction of pan-nuclear γ-H2AX signals, characterized by a diffuse phosphorylation of the H2AX histone variant throughout the entire nucleus, rather than being localized at DNA damage foci. Such phenomenon is commonly observed following high radiation doses, particularly when cells are overwhelmed by DNA damage responses [75]. Thus, although fewer γ-H2AX foci were detected, the presence of NDAus may still trigger extensive DNA damage, ultimately leading to cell death.

Regarding DNA repair (see figure 6.4C), a slight decrease was observed in cells incubated with NDAus at 2 Gy, indicating that NDAus may affect the 53BP1-mediated repair pathways. Conversely, at 6 Gy, no considerable difference was detected between control cells and those incubated with NDAus. This likely reflects the extensive DNA damage induced at high radiation doses, which inherently results in a high number of repair foci due to the intense recruitment of repair proteins. However, since 53BP1 is involved in multiple cellular processes beyond DSB repair, the foci observed under these conditions may not specifically represent the repair dynamics associated with DNA damage induced by the NDAus [76].

To further clarify this result, the colocalization of γ-H2AX and 53BP1 foci was analysed (see figure 6.4D), showing a reduced number of colocalized foci in cells incubated with

NDAus after both 2 and 6 Gy irradiation. Consistent with the previous findings, this decrease suggests that NDAus induce more complex DNA damage, which may compromise the recruitment of repair proteins to the damaged sites. Consequently, this contributes to an insufficient DNA repair capacity, leading to the markedly reduced survival of NDAus-treated cells observed in section 6.2.1.

6.3.1.2 X-rays

In line with the rationale described for γ-rays, A549 cells irradiated with 2.39 and 7.17 Gy of X-rays were imaged (see figure 6.5A) and the γ-H2AX and 53BP1 foci were quantified, both in control conditions and in the presence of NDAus at 10 μg/mL (see figure 6.5B–D).

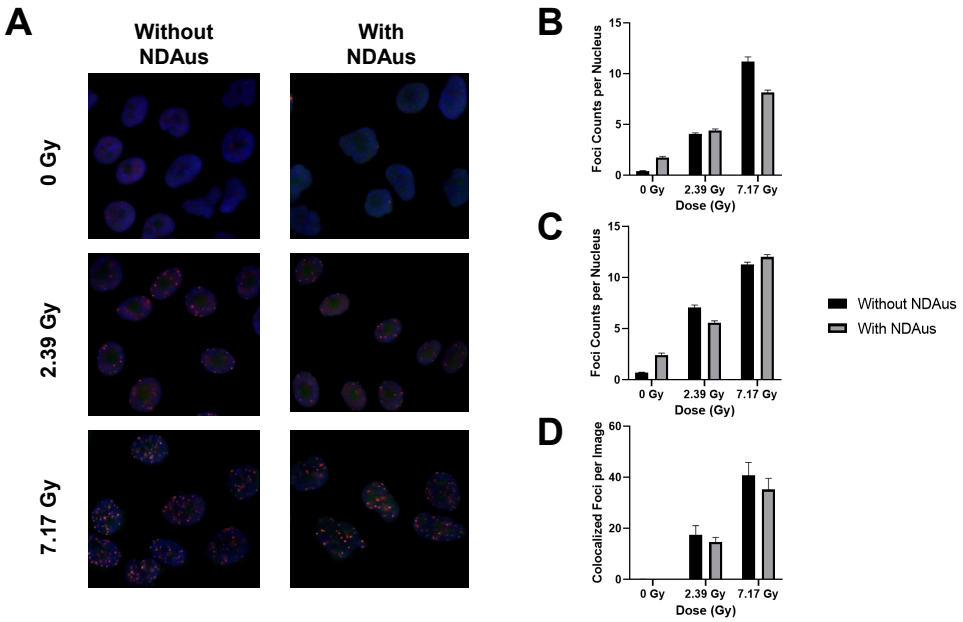

Figure 6.5: **DNA damage and repair foci following X-ray irradiation. (A)** Fluorescence microscopy images of γ-H2AX and 53BP1 foci in control cells and those incubated with NDAus after irradiation with 2.39 and 7.17 Gy. **(B)** γ-H2AX foci counts per nucleus per dose in control and NDAus-treated groups. **(C)** 53BP1 foci counts per nucleus per dose in control and NDAus-treated groups. **(D)** Colocalized γ-H2AX and 53BP1 foci per image per dose in control and NDAus-treated groups.

As illustrated in figure 6.5A, γ-H2AX and 53BP1 foci increased dependently on the radiation dose, confirming the expected induction of DSB and recruitment of repair complexes.

For the subsequent analysis, patterns similar to those observed with γ-ray irradiation were identified. Focusing on DNA damage (see figure 6.5B), the presence of NDAus did not significantly enhance the DSB formation at 2.39 Gy, as the γ-H2AX foci counts were comparable to the controls. Conversely, at 7.17 Gy, a reduction in γ-H2AX foci was detected in cells incubated with NDAus. Again, such decrease may be explained by induction of pan-nuclear γ-H2AX signals, indicating that the radiosensitizing effect is still

present, but the damage is diffused across the nucleus rather than localized in discrete foci.

Considering DNA repair (see figure 6.5C), the analysis of 53BP1 foci showed a small reduction in cells incubated with NDAus at 2 Gy, whereas at 7.17 Gy, repair foci were comparable to controls. These findings support the idea that NDAus affect the 53BP1 repair mechanisms, although such effects may be less discernible at higher radiation doses, where widespread damage recruits repair machinery broadly.

Finally, the analysis of colocalized γ-H2AX and 53BP1 foci (see figure 6.5D) revealed a decrease in colocalization for cells incubated with NDAus at 2.39 and 7.17 Gy, reinforcing the idea that NDAus induce complex DNA damage and impair the recruitment of repair proteins, ultimately contributing to the reduced cell survival reported in section 6.2.2.

6.3.1.3 Comparison of Different Radiation Type Effects

In terms of DNA damage, both radiation types produced similar numbers of γ-H2AX foci at 2.39 Gy, although at 7.17 Gy cells irradiated with X-rays exhibited a higher foci count. In addition, cells exposed to X-rays displayed fewer repair foci, in particular for 2.39 Gy, than those irradiated with γ-rays, which suggests that cells treated with X-rays developed a reduced repair capability. Moreover, cells irradiated with X-rays showed an overall higher foci colocalization. This effect can be attributed to the greater extent of damage induced by this radiation modality, which statistically increases the probability of colocalized foci formation. Taken together, these results evidence that X-rays induce greater cellular damage than γ-rays, impairing the DNA repair capability and thereby inactivating cells more efficiently.

6.3.2 ROS Production

6.3.2.1 γ-rays

While DNA damage and repair represent central endpoints of the biological response to radiation, indirect effects mediated by ROS are also key determinants of cellular radiosensitivity. Therefore, to gain a more complete perspective of how NDAus modulate the radiation effects, A549 cells irradiated with 2 and 6 Gy of γ-rays were imaged (see figure 6.6A) and the ROS fluorescence intensity was analysed, both in control conditions and in the presence of NDAus at 10 μg/mL (see figure 6.6B).

As observed in figure 6.6B, the mean ROS intensity exhibited a dose-dependent increase across all conditions, consistent with the role of ionizing radiation in promoting water radiolysis to generate ROS.

For non-irradiated cells, both control groups and cells incubated with NDAus displayed comparable ROS levels, indicating that NDAus alone do not significantly perturb the intracellular oxidative balance.

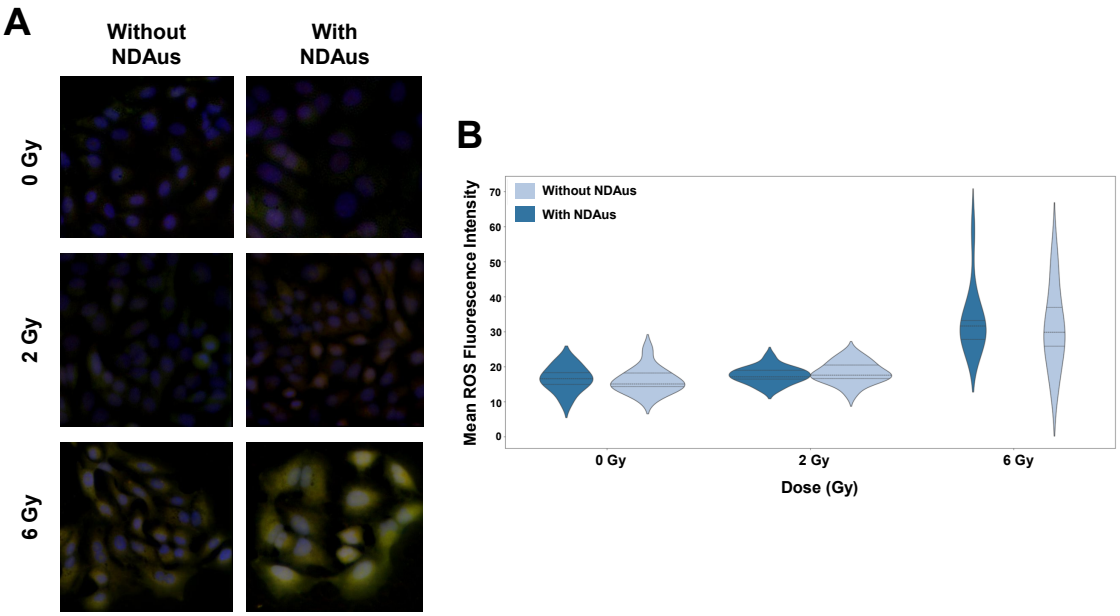

Figure 6.6: **ROS production following γ-ray irradiation. (A)** Fluorescence microscopy images of ROS production in control cells and those incubated with NDAus after irradiation with 2 and 6 Gy. **(B)** Mean ROS fluorescence intensity per dose in control and NDAus-treated groups.

Following irradiation with 2 Gy, a modest increase in ROS levels was observed for both conditions, but the difference between the two remained relatively small. This suggests that at low doses of γ-rays, the ROS production is not substantially enhanced in the presence of NDAus.

However, at 6 Gy, while ROS levels notably increased in both conditions with a wider range of values, the distribution in cells incubated with NDAus shifted toward a higher mean ROS intensity compared to controls. This indicates that NDAus enhance oxidative stress particularly under higher doses of γ-rays, where radiation-induced secondary electrons near the NDAus may interact more effectively with water molecules, catalyzing the generation of ROS.

6.3.2.2 X-rays

Consistent with the approach defined for γ-rays, A549 cells irradiated with 2.39 and 7.17 Gy of X-rays were imaged (see figure 6.7A) and the ROS fluorescence intensity was analysed, both in control conditions and in the presence of NDAus at 10 μg/mL (see figure 6.7B).

Considering figure 6.7B, the ROS intensity distributions differed according to the radiation dose and the presence of NDAus. For non-irradiated cells, the control groups and cells incubated with NDAus presented very similar ROS levels, highlighting that NDAus act as radiosensitizers rather than standalone stressors.

When cells were exposed to 2.39 Gy, both control and NDAus-incubated groups showed a rise in ROS levels. However, the distribution of ROS intensities in cells incubated

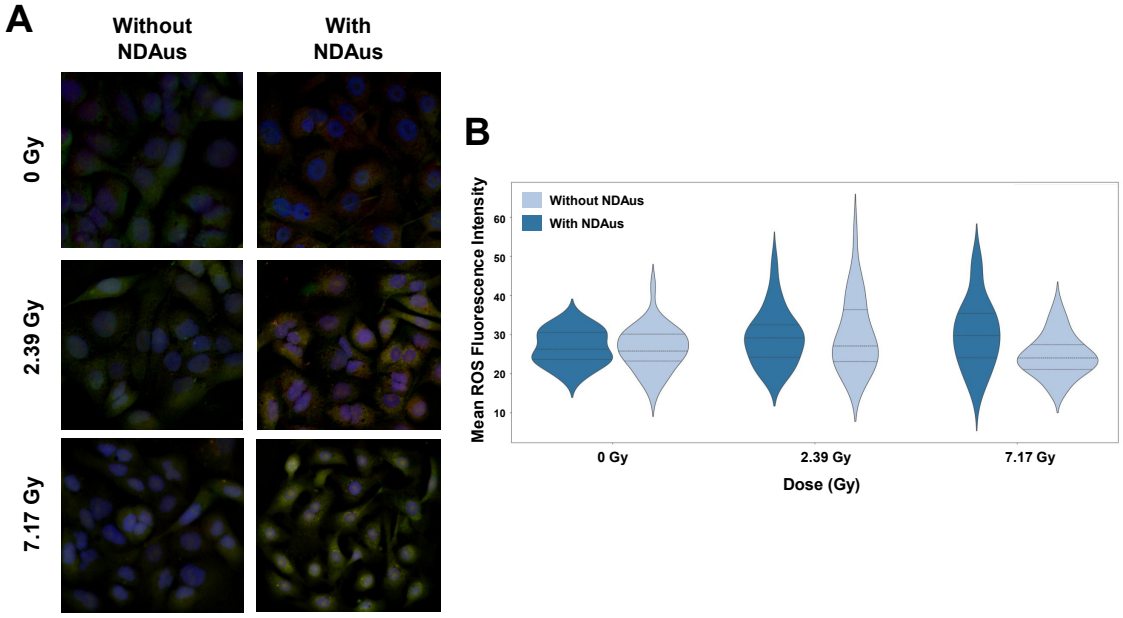

Figure 6.7: **ROS production following X-ray irradiation. (A)** Fluorescence microscopy images of ROS production in control cells and those incubated with NDAus after irradiation with 2.39 and 7.17 Gy. **(B)** Mean ROS fluorescence intensity per dose in control and NDAus-treated groups.

with NDAus presented a higher median value compared to the controls, which suggests that, under X-ray irradiation, NDAus begin to amplify secondary electron production and radical formation at clinically relevant doses.

The most striking difference between the two groups was observed at 7.17 Gy. For the control group, a narrower window of intensities was observed, with a similar median value to the same group exposed to 2.39 Gy. On the other hand, cells incubated with NDAus displayed both higher ROS intensities and a broader distribution. This pattern underscores the synergistic effect between a high dose of X-rays and the presence of NDAus, where the latter amplify the radiation damage and ultimately enhance the cellular oxidative stress.

6.3.2.3 Comparison of Different Radiation Type Effects

The ROS production exhibited distinct patterns under γ-rays and X-rays irradiation. Cells irradiated with X-rays showed a significant increase in ROS levels at 2.39 Gy, whereas those irradiated with γ-rays displayed a marked rise only at 6 Gy. This indicates that X-rays promote ROS generation at clinically relevant doses, while γ-rays require higher doses to achieve a comparable effect. Moreover, X-rays induced an overall higher ROS intensity compared to γ-rays. Together, these observations reinforce the differences between the ^{60}Co γ-rays, with two discrete MeV energies, and the LINAC X-rays, characterized by a continuous energy spectrum up to 6 MeV. In this context, the latter appear to create a more aggressive oxidative environment, particularly in the presence of NDAus, where these particles contribute more significantly to ROS production and, consequently, to enhanced cellular damage.

6.3.3 LD Formation

6.3.3.1 γ-rays

Since ROS are key mediators of oxidative damage to cellular structures, it is relevant to study if the changes observed ROS levels are accompanied by alterations in the lipid content, particularly in the cellular membrane and LD. For this purpose, A549 cells irradiated with 2 and 6 Gy of γ-rays were imaged (see figure 6.8A) and the lipid content was evaluated, both in control conditions and in the presence of NDAus at 10 μg/mL (see figure 6.8B–C).

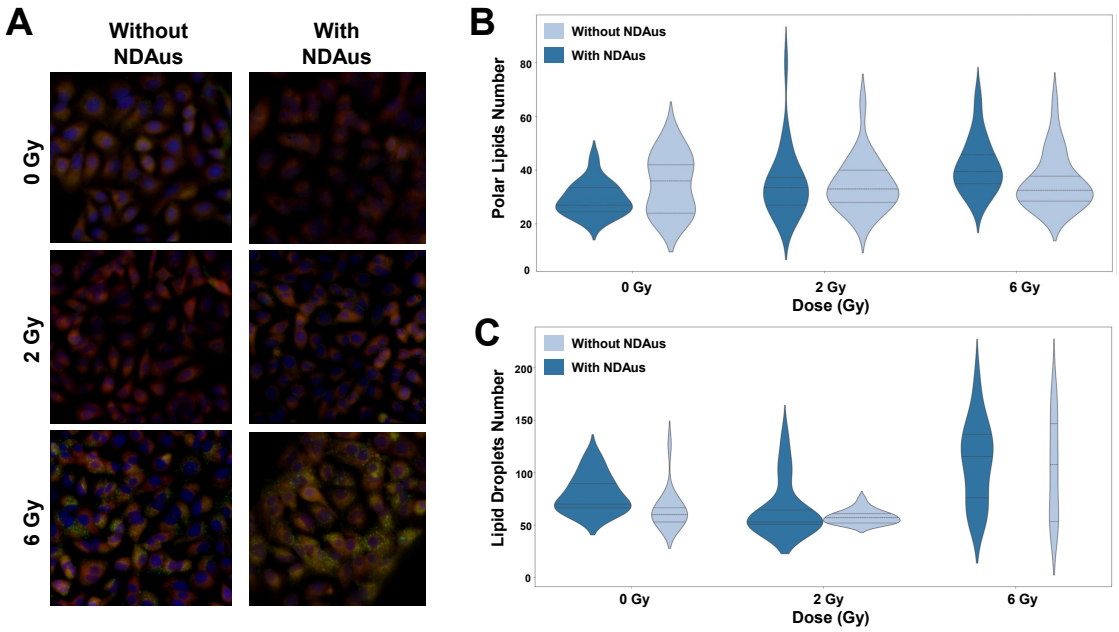

Figure 6.8: **LD formation following γ-ray irradiation. (A)** Fluorescence microscopy images of the lipid content in control cells and those incubated with NDAus after irradiation with 2 and 6 Gy. **(B)** Polar lipids number per dose in control and NDAus-treated groups. **(C)** LD number per dose in control and NDAus-treated groups.

As shown in figure 6.8B, the median number of polar lipids remained relatively stable across all conditions, suggesting that the irradiation with different doses of γ-rays and the presence of NDAus did not significantly affect the function of the lipid membrane.

Analogously, figure 6.8C shows that the number of LD was comparable between non-irradiated cells and those irradiated with 2 Gy. However, at 6 Gy, a significant increase was detected for control cells and those incubated with NDAus, but with no considerable differences between the two groups. By comparing these results with those obtained for ROS production after γ-ray irradiation (see section 6.3.2.1), a similar pattern emerges, with ROS levels increasing only at 6 Gy. This parallel suggests that ROS play a central role in lipid damage, likely through lipid peroxidation, which in turn promotes the formation of LD as a cellular defence mechanism to preserve the lipid content from further damage.

6.3.3.2 X-rays

In agreement with the approach described for γ-rays, A549 cells irradiated with 2.39 and 7.17 Gy of X-rays were imaged (see figure 6.9A) and the lipid content was evaluated, both in control conditions and in the presence of NDAus at 10 μg/mL (see figure 6.9B–C).

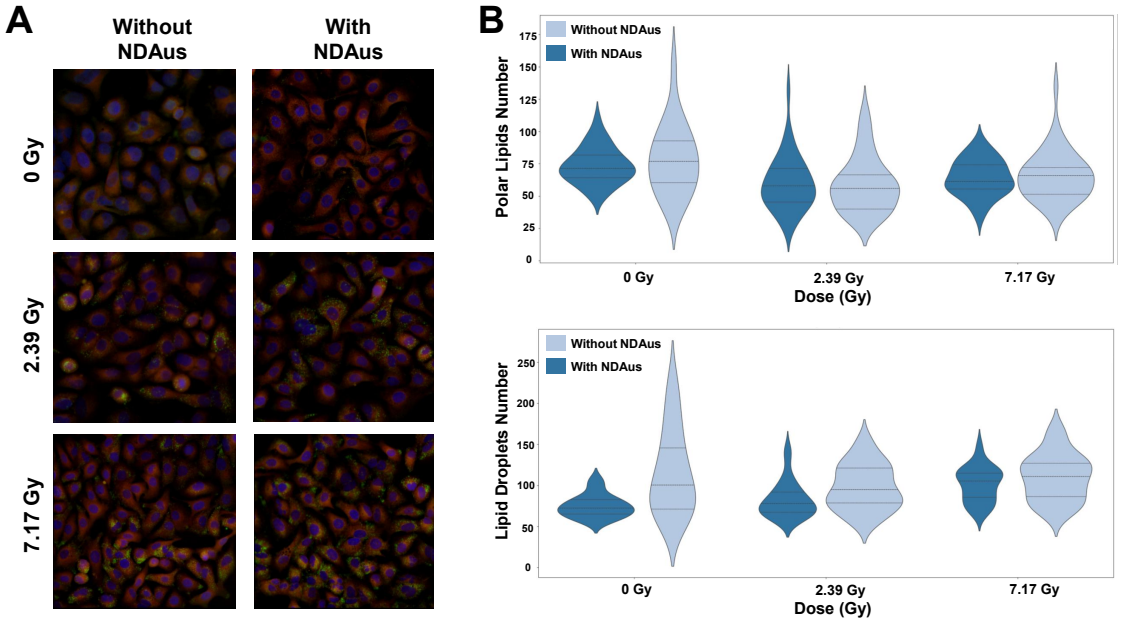

Figure 6.9: **LD formation following X-ray irradiation. (A)** Fluorescence microscopy images of the lipid content in control cells and those incubated with NDAus after irradiation with 2.39 and 7.17 Gy. **(B)** Polar lipids number per dose in control and NDAus-treated groups. **(C)** LD number per dose in control and NDAus-treated groups.

Concerning figure 6.9B, the median number of polar lipids decreased when increasing the radiation dose, with no apparent differences between control cells and those incubated with NDAus. This observation indicates that higher doses of X-rays may promote lipid degradation, which affects the integrity of cellular membranes, thereby contributing to cell damage.

In contrast, the median number of LD (see figure 6.9C) increased dependently on the dose of X-rays, again with no clear differences between control cells and those incubated with NDAus. Notably, when these findings are compared with the results obtained for ROS production after X-ray irradiation (see section 6.3.2.2), a similar trend is observed, consistent with the dose-dependent rise of ROS levels. This reinforces the notion that ROS may be the main mediators of indirect cellular damage, driving lipid remodelling processes that favor LD formation as an adaptive response to the oxidative stress induced by radiation.

6.3.3.3 Comparison of Different Radiation Type Effects

When considering the effect of both radiation types on the lipid content, different behaviors were observed. In cells irradiated with γ-rays, the number of polar lipids remained approximately stable with increasing doses, whereas in cells exposed to X-rays, the number decreased as the dose increased. This suggests that γ-rays did not substantially impact cellular membranes, while X-rays may have interacted to a greater extent with these structures, inducing further damage and promoting their degradation. Moreover, cells irradiated with X-rays exhibited an increase in LD formation at 2.39 Gy, whereas those irradiated with γ-rays only displayed a significant increase at 6 Gy, indicating that lower doses of X-rays exert an enhanced cytotoxic effect compared to γ-rays. Indeed, given the strong correlation between LD formation and ROS production for both radiation types, these results provide evidence that the oxidative stress driven by ROS may be the leading factor underlying the lipid remodelling in cells, with the latter acting as an indirect biological response to radiation.

Nevertheless, it should be noted that the presence of NDAus did not significantly affect the lipid content following irradiation, suggesting that these particles may induce cellular damage through alternative pathways. In this regard, mitochondria represent a particularly relevant target for future studies, as they play a central role in energy production, apoptosis regulation, and, in addition, are highly vulnerable to ROS-induced damage. Therefore, investigating the impact of NDAus on mitochondrial function under irradiation could provide critical insights into the mechanisms by which these nanoparticles enhance radiosensitivity, offering a valuable direction for future research.

7

Conclusion

Radiosensitizers represent a critical field in cancer research, particularly in radiotherapy, given their ability to locally amplify the radiation-induced biological effects, thereby promoting enhanced damage to cancer cells while sparing the surrounding healthy tissues.

Within this context, the present work investigated the radiosensitizing potential of NDAus in lung cancer cells exposed to different radiation types, specifically γ-rays, X-rays and protons. To this end, three fundamental experiments were conducted, including the investigation of the NDAus cellular uptake, the evaluation of cell survival following the combined treatment and the examination of radiobiological endpoints of cellular damage under the same conditions.

On this matter, cellular uptake experiments demonstrated that, when cells were incubated with NDAus at concentration of 10 μg/mL, approximately 20% of these nanoparticles available in the culture medium were internalized by cells, thus providing a reliable starting point for studying their effects under irradiation.

Regarding cell survival, similar patterns were observed under γ-ray and X-ray irradiation. Accordingly, the predominant radiosensitizing effect was obtained in cells incubated with NDAus at a concentration of 10 μg/mL, while those at 20 μg/mL displayed a behavior comparable to control cells. These results highlight the non-linear relationship between NDAus concentration and radiosensitization, which can be linked to the NDs component, as higher concentrations may favor radiation absorption rather than amplifying the radiation-induced effects. In addition, X-rays proved to be more effective in reducing cell survival when compared to γ-rays, and particularly in the presence of NDAus at 10 μg/mL. This difference can be attributed to the distinct photon energy spectra of the two radiation types, where the continuous energy distribution of X-rays enables the interaction of photons with cell components and NDAus across a broader energy range, which may induce a higher secondary electron production and, consequently, result in greater cellular damage compared with γ-rays.

Consistently, with respect to the radiobiological endpoints of cellular damage, an overall higher magnitude of cellular effects was observed under X-ray irradiation. In this context, the analysis of DNA damage and repair revealed a decreased colocalization

of γ-H2AX and 53BP1 foci in cells incubated with NDAus for both radiation modalities, highlighting that these nanoparticles induce complex DNA damage and impair the recruitment of repair proteins, ultimately contributing to a reduced cell survival. Furthermore, regarding ROS production, while γ-rays showed a significant increase of ROS levels only for high doses, the same effect was obtained for X-rays with low doses, both of which presented higher ROS distributions in NDAus groups. Moreover, focusing on the lipid content, γ-rays did not significantly affect the integrity of the cellular membranes, whereas X-rays induced a marked degradation of such structures. Equally important, while for γ-rays high radiation doses were required to increase the formation of LD, the same effect was observed for X-rays at low doses, with no significant differences between controls and NDAus groups. Given the strong correlation between LD formation and ROS levels, these results provide compelling evidence that the oxidative stress is the main driver of the lipid remodelling in irradiated cells, with X-rays creating a more aggressive oxidative environment.

On another note, it is worth mentioning that the techniques employed in this study faced some limitations, particularly in the cellular assays and irradiation procedures. In the context of cell seeding, inherent uncertainties were present given the possibility of cell aggregates in suspension, leading to non-homogeneous distributions during cell counting and pipetting, and consequently to variable numbers of seeded cells across wells. Additionally, the irradiation experiments were dependent on access to the medical LINAC at the Champalimaud Foundation and the Van de Graaff accelerator at CTN/IST, where restricted availability and maintenance schedules limited the execution of the experimental work. As a result, proton irradiation experiments could not be repeated up to this point.

As for future perspectives, proton irradiations are expected to be performed briefly, allowing to conclude on the radiosensitizing potential of NDAus under this radiation modality. Along with this, it would be valuable to investigate the DNA repair kinetics in the presence of NDAus, given that impairment of such process emerged as a key outcome of NDAus exposure. Furthermore, since mitochondria are highly susceptible to oxidative stress and central to cellular metabolism, exploring their involvement in the NDAus radiosensitizing mechanisms represents a promising direction in this research. Moreover, beyond quantifying LD formation, assessing their morphology may uncover additional insights into how the combined treatment influences the cellular lipid remodelling.

Lastly, this work was distinguished with the Young Investigator Award at the 49^{th} conference of the European Radiation Research Society, held at the Palais des Académies in Brussels, and was presented orally at that meeting. Further sharing of the findings involved an oral presentation at the 11^{th} Congress of *Proteção Contra Radiações dos Países de Língua Portuguesa*, held at the University of Coimbra, as well as the participation in the PIANOFORTE intensive course "Particle Irradiation: Molecular, Cellular and Tissue Effects", hosted by the Centre François Baclesse in Caen. These experiences reflect both the scientific contributions of this thesis and its integration into the broader international research community.

Bibliography

[1] J. M. Lourenço. *The NOVAthesis LaTeX Template User's Manual*. NOVA University Lisbon. 2021. URL: https://github.com/joaomlourenco/novathesis/raw/main/template.pdf (cit. on p. i).

[2] W. H. Organization. *Global cancer burden growing, amidst mounting need for services*. [Accessed on December 27th 2024]. URL: https://www.who.int/news/item/01-02-2024-global-cancer-burden-growing--amidst-mounting-need-for-services (cit. on p. 1).

[3] N. C. Institute. *What Is Cancer?* [Accessed on December 29th 2024]. URL: https://www.cancer.gov/about-cancer/understanding/what-is-cancer (cit. on p. 1).

[4] W. H. Organization. *Cancer*. [Accessed on January 3rd 2025]. URL: https://www.who.int/news-room/fact-sheets/detail/cancer (cit. on p. 1).

[5] N. C. Institute. *TypesCancerTreatment*. [Accessed on January 5th 2025]. URL: https://www.cancer.gov/about-cancer/treatment/types (cit. on p. 1).

[6] K. H. Kang et al. "Complications from stereotactic body radiotherapy for lung cancer". In: *Cancers* 7.2 (2015), pp. 981–1004 (cit. on p. 2).

[7] M. Césaire et al. "Radioresistance of non-small cell lung cancers and therapeutic perspectives". In: *Cancers* 14.12 (2022) (cit. on p. 2).

[8] Y.-C. Lin et al. "Multimodal bioimaging using nanodiamond and gold hybrid nanoparticles". In: *Scientific Reports* 12.1 (2022) (cit. on p. 2).

[9] E. M. Zeman, E. C. Schreiber, and J. E. Tepper. "Basics of radiation therapy". In: *Abeloff's clinical oncology*. Elsevier, 2020, pp. 431–460 (cit. on pp. 3, 5, 9).

[10] J. Herrmann. *Clinical Cardio-oncology*. Elsevier Health Sciences, 2016 (cit. on pp. 3, 10, 11).

[11] A. Fonseca. "Implementation and optimization of personalized dosimetry during targeted radionuclide therapy". MA thesis. Document delivered for the purpose of obtaining the Master's Degree at NOVA School of Science and Technology, 2022 (cit. on p. 4).

[12] J. Mott and J. Daniel. *Interactions of Electromagnetic Radiation and Subatomic Particles with Matter-Part 1*. 2021 (cit. on pp. 4, 5).

[13] J. Choi et al. "Radiosensitizing high-Z metal nanoparticles for enhanced radiotherapy of glioblastoma multiforme". In: *Journal of Nanobiotechnology* 18 (2020), pp. 1–23 (cit. on pp. 5, 12).

[14] J. Mott and J. Daniel. "Interactions of electromagnetic radiation and subatomic particles with matter–Part 2". In: *Clinical Oncology* 33.7 (2021), pp. 455–460 (cit. on p. 6).

[15] J.-s. Wang, H.-j. Wang, and H.-l. Qian. "Biological effects of radiation on cancer cells". In: *Military medical research* 5 (2018), pp. 1–10 (cit. on p. 7).

[16] Y. Khazaei Monfared et al. "DNA damage by radiopharmaceuticals and mechanisms of cellular repair". In: *Pharmaceutics* 15.12 (2023) (cit. on p. 7).

[17] S. Penninckx et al. "Quantification of radiation-induced DNA double strand break repair foci to evaluate and predict biological responses to ionizing radiation". In: *NAR cancer* 3.4 (2021) (cit. on p. 7).

[18] S. Jia et al. "Promoting reactive oxygen species generation: a key strategy in nanosensitizer-mediated radiotherapy". In: *Nanomedicine* 16.9 (2021), pp. 759–778 (cit. on p. 8).

[19] J.-P. Pouget et al. "Introduction to radiobiology of targeted radionuclide therapy". In: *Frontiers in medicine* 2 (2015) (cit. on p. 8).

[20] L. F. Ye et al. "Radiation-induced lipid peroxidation triggers ferroptosis and synergizes with ferroptosis inducers". In: *ACS chemical biology* 15.2 (2020), pp. 469–484 (cit. on p. 8).

[21] A. W. Girotti. "Photosensitized oxidation of membrane lipids: reaction pathways, cytotoxic effects, and cytoprotective mechanisms". In: *Journal of Photochemistry and Photobiology B: Biology* 63.1-3 (2001), pp. 103–113 (cit. on p. 8).

[22] Y. Jin et al. "Lipid droplets: A cellular organelle vital in cancer cells". In: *Cell death discovery* 9.1 (2023) (cit. on p. 8).

[23] E. Jarc and T. Petan. "Lipid droplets and the management of cellular stress". In: *The Yale journal of biology and medicine* 92.3 (2019) (cit. on p. 8).

[24] M. De Martino et al. "Radiation therapy promotes unsaturated fatty acids to maintain survival of glioblastoma". In: *Cancer Letters* 570 (2023) (cit. on p. 8).

[25] L. Tirinato et al. "Lipid droplets and ferritin heavy chain: a devilish liaison in human cancer cell radioresistance". In: *Elife* 10 (2021) (cit. on p. 8).

[26] F. Pagliari et al. "Cancer radioresistance is characterized by a differential lipid droplet content along the cell cycle". In: *Cell Division* 19.1 (2024) (cit. on p. 8).

[27] L. Gong et al. "Application of radiosensitizers in cancer radiotherapy". In: *International journal of nanomedicine* (2021), pp. 1083–1102 (cit. on pp. 9, 11).

[28] R. Baskar et al. "Cancer and radiation therapy: current advances and future directions". In: *International journal of medical sciences* 9.3 (2012) (cit. on pp. 8, 11).

[29] B. Healy et al. "Cobalt-60 machines and medical linear accelerators: competing technologies for external beam radiotherapy". In: *Clinical Oncology* 29.2 (2017), pp. 110–115 (cit. on p. 9).

[30] J. S. Vaidya. "Principles of cancer treatment by radiotherapy". In: *Surgery (Oxford)* 39.4 (2021), pp. 193–201 (cit. on p. 9).

[31] E. Podgorsak. *Radiation Oncology Physics: A Handbook for Teachers and Students*. Elsevier, 2005 (cit. on p. 10).

[32] J. R. Cunningham. "Cobalt-60 Units for Radiotherapy". In: *Encyclopedia of Medical Devices and Instrumentation* 2 (2006), pp. 120–133 (cit. on p. 9).

[33] H.-U. Kauczor and T. Bäuerle. *Imaging of complications and toxicity following tumor therapy*. Tech. rep. Springer, 2015 (cit. on p. 10).

[34] R. Mohan. "A review of proton therapy–Current status and future directions". In: *Precision radiation oncology* 6.2 (2022), pp. 164–176 (cit. on p. 10).

[35] A. R. Smith. "Proton therapy". In: *Physics in Medicine & Biology* 51.13 (2006) (cit. on p. 10).

[36] F. Boateng and W. Ngwa. "Delivery of nanoparticle-based radiosensitizers for radiotherapy applications". In: *International journal of molecular sciences* 21.1 (2019) (cit. on p. 11).

[37] N. Jackson et al. "Application of High-Z Nanoparticles to Enhance Current Radiotherapy Treatment". In: *Molecules* 29.11 (2024) (cit. on pp. 11, 12).

[38] A. Marques et al. "Dose rate effects on the selective radiosensitization of prostate cells by GRPR-targeted gold nanoparticles". In: *International Journal of Molecular Sciences* 23.9 (2022) (cit. on p. 11).

[39] C. Bilynsky, N. Millot, and A.-L. Papa. "Radiation nanosensitizers in cancer therapy—From preclinical discoveries to the outcomes of early clinical trials". In: *Bioengineering & Translational Medicine* 7.1 (2022) (cit. on p. 11).

[40] Arnida, A. Malugin, and H. Ghandehari. "Cellular uptake and toxicity of gold nanoparticles in prostate cancer cells: a comparative study of rods and spheres". In: *Journal of Applied Toxicology: An International Journal* 30.3 (2010), pp. 212–217 (cit. on p. 11).

[41] B. D. Chithrani, A. A. Ghazani, and W. C. Chan. "Determining the size and shape dependence of gold nanoparticle uptake into mammalian cells". In: *Nano letters* 6.4 (2006), pp. 662–668 (cit. on p. 11).

[42] B. B. Abdollahi et al. “Main approaches to enhance radiosensitization in cancer cells by nanoparticles: A systematic review”. In: *Advanced pharmaceutical bulletin* 11.2 (2020) (cit. on p. 12).

[43] C.-Y. Lo et al. “Gold-Nanoparticles-Enhanced Production of Reactive Oxygen Species in Cells at Spread-Out Bragg Peak under Proton Beam Radiation”. In: *ACS Omega* 8.20 (2023), pp. 17922–17931 (cit. on p. 12).

[44] J.-X. Qin et al. “Nanodiamonds: Synthesis, properties, and applications in nanomedicine”. In: *Materials & Design* 210 (2021) (cit. on p. 13).

[45] P. Aprà et al. “Interaction of nanodiamonds with water: impact of surface chemistry on hydrophilicity, aggregation and electrical properties”. In: *Nanomaterials* 11.10 (2021) (cit. on p. 13).

[46] S. Kumar et al. “Nanodiamonds: Emerging face of future nanotechnology”. In: *Carbon* 143 (2019), pp. 678–699 (cit. on p. 13).

[47] A. Santos. “Recent progress in biomedical applications of nanodiamonds”. In: *Instituto de Arquitectura Diseño y Arte* (2018) (cit. on p. 13).

[48] F. Yoshino et al. “Preferential tumor accumulation of polyglycerol functionalized nanodiamond conjugated with cyanine dye leading to near-infrared fluorescence in vivo tumor imaging”. In: *Small* 15.48 (2019) (cit. on p. 13).

[49] S. Sturari et al. “Designing Functionalized Nanodiamonds with Hyaluronic Acid-Phospholipid Conjugates for Enhanced Cancer Cell Targeting and Fluorescence Imaging Capabilities”. In: *Nanoscale* (2024) (cit. on p. 13).

[50] Z. Mi et al. “Quantifying nanodiamonds biodistribution in whole cells with correlative iono-nanoscopy”. In: *Nature Communications* 12.1 (2021) (cit. on pp. 13, 14).

[51] R. Grall et al. “Impairing the radioresistance of cancer cells by hydrogenated nanodiamonds”. In: *Biomaterials* 61 (2015), pp. 290–298 (cit. on p. 14).

[52] V. Varzi et al. “Nanodiamond Effects on Cancer Cell Radiosensitivity: The Interplay between Their Chemical/Physical Characteristics and the Irradiation Energy”. In: *International Journal of Molecular Sciences* 24.23 (2023) (cit. on pp. 14, 18, 28).

[53] S. Orlanducci. “Gold-Decorated Nanodiamonds: Powerful Multifunctional Materials for Sensing, Imaging, Diagnostics, and Therapy”. In: *European Journal of Inorganic Chemistry* 2018.48 (2018), pp. 5138–5145 (cit. on p. 15).

[54] E. Mendes et al. “Synthesis and characterization of gold-coated nanodiamonds through green chemistry as potential radiosensitizers for proton therapy”. In: *arXiv preprint* (2025) (cit. on p. 15).

[55] W. Liu et al. “Fluorescent nanodiamond–gold hybrid particles for multimodal optical and electron microscopy cellular imaging”. In: *Nano letters* 16.10 (2016), pp. 6236–6244 (cit. on p. 15).

[56] N. A. Franken et al. "Clonogenic assay of cells in vitro". In: *Nature protocols* 1.5 (2006), pp. 2315–2319 (cit. on p. 16).

[57] L. Dobešová et al. "Incorporation of low concentrations of gold nanoparticles: complex effects on radiation response and fate of cancer cells". In: *Pharmaceutics* 14.1 (2022) (cit. on p. 16).

[58] S. J. McMahon. "The linear quadratic model: usage, interpretation and challenges". In: *Physics in Medicine & Biology* 64.1 (2018) (cit. on pp. 16, 27, 56).

[59] A. Subiel, R. Ashmore, and G. Schettino. "Standards and methodologies for characterizing radiobiological impact of high-Z nanoparticles". In: *Theranostics* 6.10 (2016) (cit. on p. 17).

[60] E. Mendes. "New radiosensitizer platforms for proton therapy: boronated compounds and gold-coated nanodiamonds". MA thesis. Document delivered for the purpose of obtaining the Master's Degree at Instituto Superior Técnico, 2024 (cit. on p. 18).

[61] A. Marques. "Evaluation of the Radiosensitizing Capabilities of Target-Specific Gold Nanoparticles in the Radiotherapy of Prostate Cancer". MA thesis. Document delivered for the purpose of obtaining the Master's Degree at Instituto Superior Técnico, 2021 (cit. on p. 19).

[62] A. Martins. "Investigation of the Potential of Concomitant Radiation Therapy with Gold Nanoparticles for Pancreatic Cancer". MA thesis. Document delivered for the purpose of obtaining the Master's Degree at Faculdade de Ciências da Universidade de Lisboa, 2022 (cit. on p. 20).

[63] T. Almeida. "Design of a phantom for radiobiology studies". MA thesis. Document delivered for the purpose of obtaining the Master's Degree at Faculdade de Ciências da Universidade de Lisboa, 2022 (cit. on p. 20).

[64] B. P. McCabe et al. "Calibration of GafChromic XR-RV3 radiochromic film for skin dose measurement using standardized x-ray spectra and a commercial flatbed scanner". In: *Medical physics* 38.4 (2011), pp. 1919–1930 (cit. on p. 21).

[65] H. Kim and X. Xue. "Detection of total reactive oxygen species in adherent cells by 2′, 7′-dichlorodihydrofluorescein diacetate staining". In: *Journal of visualized experiments: JoVE* 160 (2020), pp. 10–3791 (cit. on p. 22).

[66] P. Greenspan, E. P. Mayer, and S. D. Fowler. "Nile red: a selective fluorescent stain for intracellular lipid droplets." In: *The Journal of cell biology* 100.3 (1985), pp. 965–973 (cit. on p. 23).

[67] B. B. Abdollahi et al. "Main approaches to enhance radiosensitization in cancer cells by nanoparticles: A systematic review". In: *Advanced pharmaceutical bulletin* 11.2 (2020) (cit. on p. 26).

[68] K. Butterworth et al. “Evaluation of cytotoxicity and radiation enhancement using 1.9 nm gold particles: potentialapplication for cancer therapy”. In: *Nanotechnology* 21.29 (2010) (cit. on p. 26).

[69] C. M. Van Leeuwen et al. “The alfa and beta of tumours: a review of parameters of the linear-quadratic model, derived from clinical radiotherapy studies”. In: *Radiation oncology* 13.1 (2018) (cit. on p. 27).

[70] T. Matsui et al. “Robustness of clonogenic assays as a biomarker for cancer cell radiosensitivity”. In: *International journal of molecular sciences* 20.17 (2019) (cit. on p. 27).

[71] R. H. Millares et al. “Clonogenic assay and computational modeling using real cell images to study physical enhancement and cellular sensitization induced by metal nanoparticles under MV and kV X-ray irradiation”. In: *Nanoscale* 16.14 (2024), pp. 7110–7122 (cit. on p. 27).

[72] E. Shahhoseini et al. “Determination of dose enhancement caused by AuNPs with Xoft® Axxent® Electronic (eBx™) and conventional brachytherapy: in vitro study”. In: *International journal of nanomedicine* (2018), pp. 5733–5741 (cit. on p. 27).

[73] I. Tremi et al. “Biological response of human cancer cells to ionizing radiation in combination with gold nanoparticles”. In: *Cancers* 14.20 (2022) (cit. on p. 27).

[74] S. Penninckx et al. “The role of thioredoxin reductase in gold nanoparticle radiosensitization effects”. In: *Nanomedicine* 13.22 (2018), pp. 2917–2937 (cit. on p. 27).

[75] D. Ding et al. “Induction and inhibition of the pan-nuclear gamma-H2AX response in resting human peripheral blood lymphocytes after X-ray irradiation”. In: *Cell death discovery* 2.1 (2016), pp. 1–10 (cit. on p. 31).

[76] E. Pariset et al. “53BP1 repair kinetics for prediction of in vivo radiation susceptibility in 15 mouse strains”. In: *Radiation Research* 194.5 (2020), pp. 485–499 (cit. on p. 31).

[77] B. Alves. “Modelação biofísica e simulação de nanoplataformas multifuncionais de B/Fe para terapia com protões”. MA thesis. Document delivered for the purpose of obtaining the Master’s Degree at Faculdade de Ciências da Universidade de Lisboa, 2024 (cit. on p. 57).

A

Laboratory Protocols

A.1 Clonogenic Assay Protocol

A.1.1 Materials and Reagents

- DMEM culture medium (Dulbecco's modified Eagle's medium)
- PBS
- Methanol
- Glacial acetic acid
- Giemsa solution 4%

A.1.2 Procedure

1. **Cell Seeding and Treatment**

   a) Seed cells.

   b) 24h after seeding, remove the medium and incubate cells with NDAus for 24h.

   c) Remove NDAus and add 400 μL per well of fresh medium.

   d) Irradiate cells in fresh medium.

   e) Leave the cells in the incubator for ten days and replace the medium with fresh one on the fifth day.

2. **Fixation and Staining of Colonies**
   Fixation Solution:

   - Prepare Carnoy's fixative fresh on the day of use. Solution consists of 3 parts metanol to 1 part glacial acetic acid. Leave the solution on the freezer for 1 hour. Note: Prepare enough solution to fix all cultures.

   Fixation of Colonies:

a) Remove the medium above the cells.

b) Rinse carefully with 500μL of PBS.

c) Add 500 μL of Carnoy's solution for 20 minutes at RT.

d) Remove the solution and leave the culture dishes to dry.

Staining Solution of Giemsa 4%:
Stock Giemsa solution: Commercial Giemsa stain is usually 100% concentrated in methanol. Dilution to 4% Working Solution:

- Mix 4 mL of Giemsa stock solution with 96 mL of buffer/distilled water (pH 6.8). Ensure proper mixing before use.

Staining of Colonies:

a) Add 500 μL of staining solution for 15 to 25 minutes at RT.

b) Remove the solution and wash with water.

c) Leave the dishes with colonies to dry at RT.

d) Count the colonies with a pen.

e) Calculate the PE and SF.

A.2 DNA Damage and Repair Assay Protocol

A.2.1 Materials and Reagents

Cell Culture and Fixation

- DMEM culture medium (Dulbecco's modified Eagle's medium)
- Coverslips
- PBS
- PFA 4%
- 0.5% Triton X-100 (for permeabilization)

Antibodies and Buffers

- Blocking buffer: 2% BSA in PBS
- DAPI (nuclear stain)
- Mounting medium (e.g. ProLong Gold Antifade)

a) Primary Antibodies

- γ-H2AX (Ser139) (Mouse, Millipore)
- 53BP1 (Rabbit, e.g., Invitrogen)

b) Secondary Antibodies

- Alexa Fluor 488 (Anti-Mouse)
- Texas-Red (Anti-Rabbit)

A.2.2 Procedure

1. **Cell Seeding and Treatment**

   a) Seed cells.

   b) 24h after seeding, remove the medium and incubate cells with NDAus for 24h.

   c) Remove NDAus and add 400 μL per well of fresh medium.

   d) Irradiate cells in fresh medium.

2. **Fixation and Permeabilization**

   Fix cells:

i. 4% PFA (15 min, Room Temperature (RT)) + wash with PBS.
Final volume of 1 mL: 250 μL of PFA + 750 μL of PBS (1x, non-sterile).

ii. Permeabilize with 0.5% Triton X-100 (5 min, RT) – Cold Solution
Final volume of 1 mL: 5 μL of Triton + 995 μL of PBS (1x, non-sterile)

iii. Wash 3x with PBS (1x, non-sterile).

3. **Blocking**

   i. Incubate cells with blocking buffer (2% BSA in PBS) for 15 minutes at RT.
   Total volume of 50 mL: 1 g of BSA + 50 mL of PBS (1x, non-sterile).

4. **Primary Antibody Staining** (Dilute primary antibodies in blocking buffer)

   i. Incubate 1h, at RT, with γ-H2AX and 53BP1 antibodies (Range for dilutions in blocking buffer: 1:500 – 1:1000).
   Dilution of 1/800 (total volume 1 mL): 1.2 μL h2ax + 1.2 μL 53BP1 + 997.6 μL blocking buffer (2% BSA in PBS).

   ii. Wash cells 3x with PBS (1x, non-sterile).

5. **Secondary Antibody Staining** (Dilute secondary antibodies in blocking buffer)

   i. Incubate 1h, at RT, with fluorescent secondary antibodies (1:1000 in PBS) – In the dark.
   Dilution of 1/1000 (total volume 1 mL): 1 μL Alexa-Fluor (anti-mouse) + 1 μL Texas-Red (anti-rabbit) + 998 μL blocking buffer (2% BSA in PBS).

   ii. Wash 3x with PBS (1x, non-sterile).

6. **Nuclear Staining Mounting**

   i. Stain nuclei with DAPI (1:5000 in PBS, 5 min, RT).

   ii. Wash 3x with PBS.

   iii. Mount coverslips on slides using ProLong Gold Antifade.

   iv. Let dry overnight at RT in the dark.

   DAPI preparation:

   - Aliquot −20°C: 10 mL + 10 mL H2Od.
   - Dilution of 1/25: 1200 μL + 30 ml PBS.

   Or

   - Mount coverslips on slides using ProLong Gold Antifade+DAPI.
   - Let dry overnight at RT in the dark.

7. **Imaging and Colocalization Analysis**

i. Use a confocal or widefield fluorescence microscope.

   Excitation/emission filters:

   - γ-H2AX (Alexa 488, Green) $\rightarrow$ Excite at 488 nm
   - DAPI (Blue) $\rightarrow$ Excite at 405 nm
   - TR (red) $\rightarrow$ Excite at 595 nm

ii. Capture Z-stack images if needed for 3D nuclear foci analysis.

iii. Analyze colocalization with ImageJ/Fiji (JACoP plugin) or CellProfiler

A.2.3 Expected Results

- γ-H2AX forms nuclear foci at DNA double-strand breaks.

- 53BP1 foci should overlap (colocalize) with γ-H2AX, forming yellow signals in merged images.

- In DNA repair-deficient cells, fewer or altered foci may be observed.

A.2.4 General Tips

- Prepare a fresh 4% PFA solution prior to fixation. 4% PFA can be stored at $-20°C$ for less than 3 months.

- Do not dry the cells during the entire process.

- It is recommended to optimize the working concentration of antibody. The reactivity may vary due to lot-to-lot variability.

- Before adding antibodies to the staining buffer, briefly centrifuge and use only the supernatant. The antibody may be precipitated.

- Phalloidin staining is not compatible with alcohol-based (e.g., ice-cold methanol) or acid-based (e.g., trichloroacetic acid) fixation and is not compatible with most enzymatic or heatinduced epitope retrieval processes.

A.3 ROS Production Assay Protocol

A.3.1 Materials and Reagents

- DCFH-DA (2',7'-dichlorodihydrofluorescein diacetate)
- DMEM culture medium (Dulbecco's modified Eagle's medium)
- PBS

A.3.2 Procedure

1. Seed cells.
2. 24h after seeding, remove the medium and incubate cells with NDAus for 24h.
3. Remove NDAus and add 400 μL per well of fresh medium.
4. Irradiate cells in fresh medium.
5. After irradiation, add 400 μL/well of PFA solution (4%) for 15 minutes.
   Final volume of 1 mL: 250 μL of PFA + 750 μL of PBS (1x, non-sterile).
6. Remove the solution and wash with PBS (1x, non-sterile).
7. Incubate with 10 μM DCFH-DA (400 μLper well) for 30 minutes in the dark.
8. Wash with PBS (1x, non-sterile).

   Nuclear Staining and Mounting

   i. Stain nuclei with DAPI (1:5000 in PBS, 5 min, RT).
   ii. Wash 3x with PBS.
   iii. Mount coverslips on slides using ProLong Gold Antifade.
   iv. Let dry overnight at RT in the dark.

   DAPI Preparation

   - Aliquot −20°C: 10 mL + 10 mL H2Od.
   - Dilution of 1/25: 1200 μL + 30 ml PBS.

   Or

   - Mount coverslips on slides using ProLong Gold Antifade+DAPI.
   - Let dry overnight at RT in the dark.

9. Remove the coverslip with cells from the well and collocate into a clean slide.

10. Put a coverslip covering the slide.

11. Analyze the cells with a fluorescence microscope using FITC filter.

A.3.3 Reagent Preparation

DCFH-DA (10 mL): Add 10 μL of DCFH-DA to 9990 μL of DMEM.

A.4 LD Formation Assay Protocol

A.4.1 Materials and Reagents

- Nile Red (9-diethylamino-5H-benzo[a]phenoxazine-5-1)
- DMEM culture medium (Dulbecco's modified Eagle's medium)
- PBS

A.4.2 Procedure

1. Seed cells.
2. 24h after seeding, remove the medium and incubate cells with NDAus for 24h.
3. Remove NDAus medium and add 400 μL per well of fresh medium. Irradiate cells in fresh medium.
4. After irradiation, add 400 μL/well of PFA solution (4%) for 15 minutes.
5. Remove the solution and wash with PBS (1x).
6. Incubate with 400 μL/well of Nile Red working solution and incubate for 15 to 30 min at room temperature in the dark.
7. Remove the solution and wash cells with PBS (2–3 x) to remove unbound dye.

   Nuclear Staining and Mounting

   i. Stain nuclei with DAPI (1:5000 in PBS, 5 min, RT).
   ii. Wash 3x with PBS.
   iii. Mount coverslips on slides using ProLong Gold Antifade.
   iv. Let dry overnight at RT in the dark.

   DAPI Preparation

   - Aliquot −20°C: 10 mL + 10 mL H2Od.
   - Dilution of 1/25: 1200 μL + 30 ml PBS.

   Or

   - Mount coverslips on slides using ProLong Gold Antifade+DAPI.
   - Let dry overnight at RT in the dark.

8. Remove the coverslip with cells from the well and collocate into a clean slide.

9. Put a coverslip covering the slide.
10. Analyze the cells with a fluorescence microscope using TXR and FITC filter.

A.4.3 Stock Solution and Working Solution Preparation

Stock Solution: Nile red solution in dimethylsulfoxide (DMSO) 30 mM; −20°C.

Working Solution: Equilibrate NR stock solution to room temperature.

1. Dilute the stock NR 1:10 in PBS (10 μL of stock NR solution + 90 μL of PBS) – NRs-1 solution.
2. Dilute NRs-1 1:300 in PBS (30 μL of NRs-1 + 8970 μL of PBS).

A.4.4 Imaging Analysis

- Neutral lipids (lipid droplets) → Excite at 450–500 nm, yellow-green emission.
- Polar lipids (membrane lipids) → Excite at 515–560 nm, orange-red emission.
- DAPI counterstain (nuclei, optional) → Excite at 405 nm, blue emission.

A.4.5 Expected Results

- Lipid droplets appear bright yellow-green under the microscope.
- Polar lipids appear orange-red under the microscope.
- Increased Nile Red intensity indicates higher lipid accumulation in cells.

I

Annexes

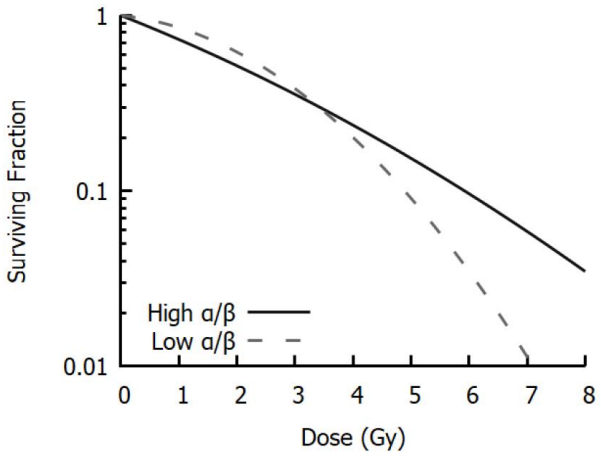

Figure I.1: **Survival curves fitted with the LQ model of cells with high and low α/β ratios.** Adapted from [58].

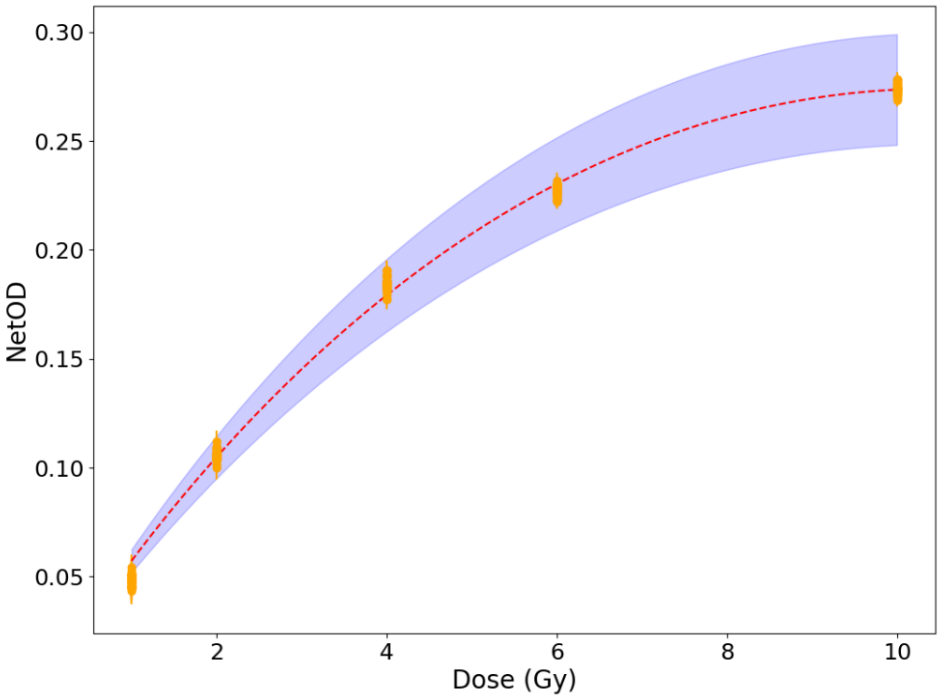

Figure I.2: **Calibration curve for proton dosimetry using Gafchromic XR-RV3 radiochromic films.** Adapted from [77].

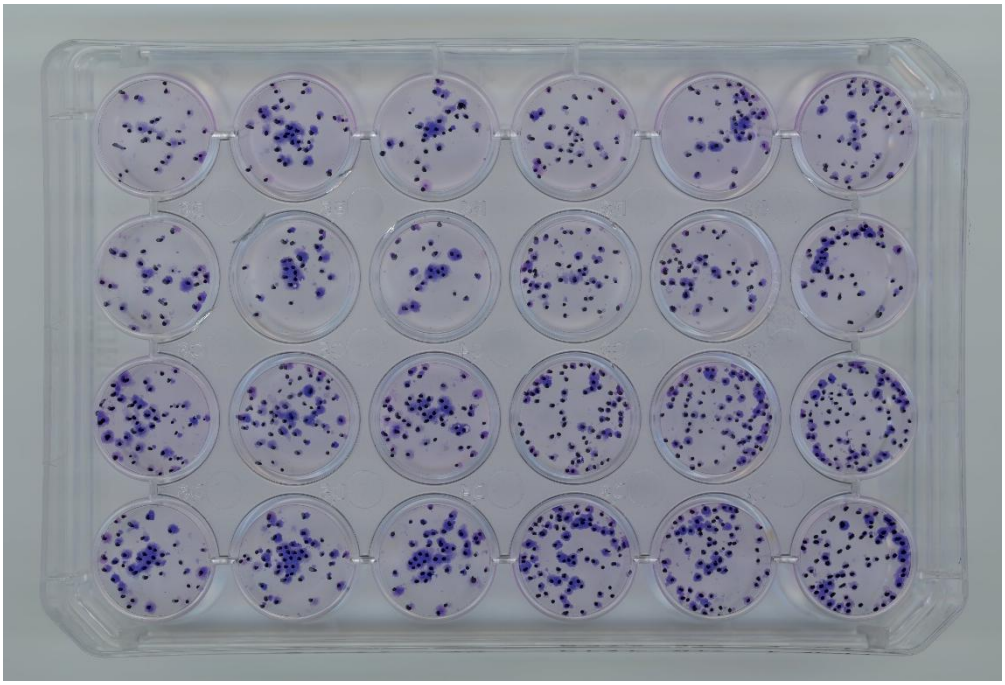

Figure I.3: **Stained and counted A549 cell colonies in a 24-well plate after the clonogenic assay.**

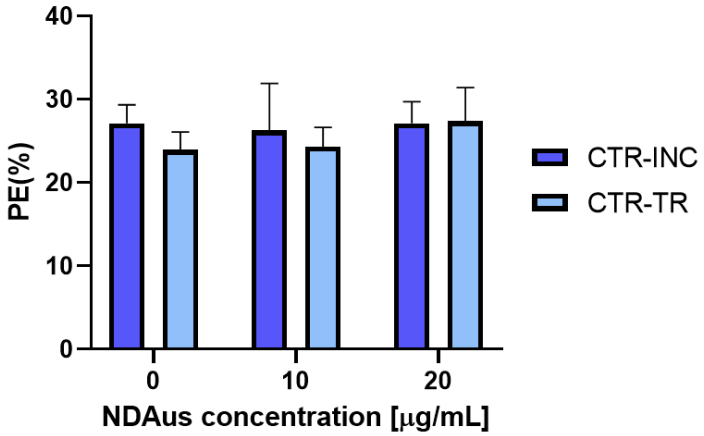

Figure I.4: **PE of A549 control cells and those incubated with NDAus at concentrations of 10 and 20 μg/mL when transported from CTN/IST to Champalimaud Foundation and back (CTR-TR), and when left at the incubator at CTN/IST (CTR-INC).**

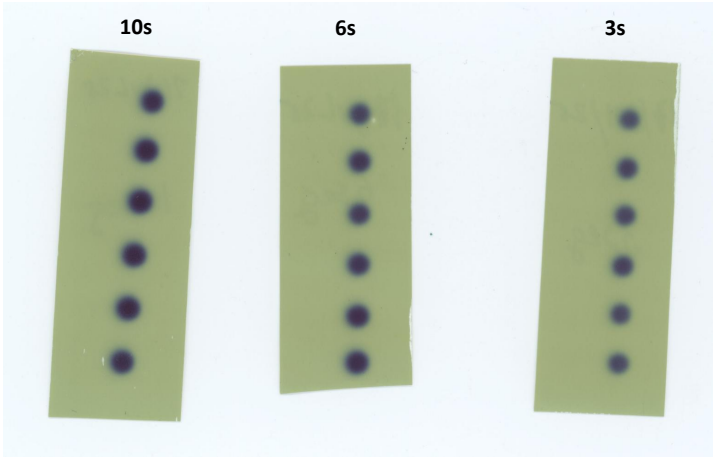

Figure I.5: **Gafchromic XR-RV3 radiochromic films irradiated with a proton beam during 3, 6 and 10 seconds.**

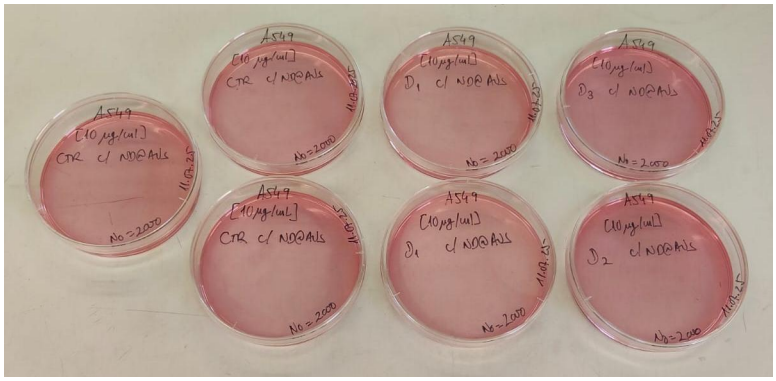

Figure I.6: **Petri dishes showing the absence of cell colony formation after proton irradiation.**

Table I.1: Physiological elements present in the cell matrix of A549 control cells and those incubated with NDAus at 10 μg/mL, expressed in μg per 10^6 cells.

	Physiological Elements (Mean ± SD)						
	Phosphorus (P)	Sulfur (S)	Chlorine (Cl)	Potassium (K)	Calcium (Ca)	Iron (Fe)	Zinc (Zn)
A549 control cells	46 ± 4	21 ± 2	370 ± 20	57 ± 5	2.02 ± 0.05	0.3 ± 0.2	0.33 ± 0.05
A549 cells with NDAus [10μg/mL]	49 ± 2	21.0 ± 0.4	220 ± 30	74 ± 5	3.7 ± 0.6	0.4 ± 0.2	0.37 ± 0.07

Table I.2: **Survival fractions of A549 control cells and those incubated with NDAus at concentrations of 10 and 20 μg/mL after γ-ray irradiation at doses ranging from 0.5 to 10 Gy.**

Dose (Gy)	**Survival Fraction**								
	CTR			NDAus [20 μg/mL]			NDAus [10 μg/mL]		
	A1	A2	A3	A1	A2	A3	A1	A2	A3
0.0	1.000	1.000	1.000	1.000	1.000	1.000	1.000	1.000	1.000
0.5	0.547	0.924	0.780	0.427	0.998	0.867	0.644	0.978	0.720
1.0	0.796	0.841	1.321	0.737	0.916	1.237	0.769	0.883	1.164
2.0	0.889	0.759	1.193	0.655	0.835	1.077	0.638	0.796	0.924
4.0	0.594	0.610	0.560	0.539	0.732	0.533	0.445	0.676	0.514
6.0	0.238	0.362	0.251	0.314	0.410	0.252	0.294	0.425	0.201
8.0	0.073	0.113	0.130	0.070	0.158	0.104	0.044	0.132	0.100
10.0	0.024	0.038	0.033	0.023	0.053	0.014	0.047	0.058	0.041

Table I.3: **Survival fractions of A549 control cells and those incubated with NDAus at concentrations of 10 and 20 μg/mL after X-ray irradiation at doses ranging from 0.5 to 8 Gy.**

Dose (Gy)	**Survival Fraction**								
	CTR			NDAus [20 μg/mL]			NDAus [10 μg/mL]		
	A1	A2	A3	A1	A2	A3	A1	A2	A3
0.0	1.000	1.000	1.000	1.000	1.000	1.000	1.000	1.000	1.000
0.5	0.770	0.929	1.072	0.747	0.893	0.982	0.820	0.778	0.899
1.0	0.632	0.825	0.985	0.611	0.799	0.830	0.671	0.566	0.827
2.0	0.626	0.647	0.697	0.656	0.528	0.618	0.601	0.545	0.535
4.0	0.151	0.280	0.420	0.152	0.227	0.269	0.101	0.222	0.270
6.0	0.030	0.082	0.119	0.030	0.040	0.076	0.022	0.035	0.089
8.0	0.005	0.009	0.038	0.008	0.008	0.016	0.003	0.005	0.005

2025

Evaluating the Potential of Gold-coated Nanodiamonds as Radiosensitizers to Enhance the Effectiveness of Radiation Therapy

Gil Alves

NOVA

NOVA SCHOOL OF SCIENCE & TECHNOLOGY